Er-W codoping of TiO$_2$-anatase: Structural and electronic characterization and disinfection capability under UV–vis, and near-IR excitation

Anna Kubacka*, Mario J. Muñoz-Batista, Manuel Ferrer, Marcos Fernández-Garcia*

Instituto de Catálisis y Petroleoquímica, CSIC, C/Marie Curie 2, 28049, Madrid, Spain

ABSTRACT

The codoping of the anatase structure with tungsten and erbium was carried out using a microemulsion preparation procedure. Tungsten and erbium single doped and pure anatase nanomaterials were also prepared. The corresponding solids were characterized using X-ray diffraction, surface area, transmission electron microscopy, X-ray photoelectron and absorption (X-ray near-edge and extended X-ray absorption) spectroscopies as well as UV–vis and photoluminescence spectroscopies. Results provided a complete structural and electronic characterization of the solids, showing the unique features generated by the copresence of tungsten and erbium at substitutional positions of the anatase structure. The disinfection capability of these single and codoped TiO$_2$-based materials was tested against Gram-negative (*Escherichia coli*) and Gram-positive (*Staphylococcus aureus*) bacteria and under ultraviolet, visible and near infrared light excitations. The ErW-anatase solid presents significant photoactivity in the elimination of both microorganisms in the whole UV–vis-nearIR range of excitation wavelengths. The biocidal results were interpreted with the help of a kinetic modelling of the experiments and correlated with results from the physico-chemical characterization of the samples and from an electron paramagnetic resonance and optical study of the radicals species produced under illumination. This procedure indicates a different physical origin of the photoactivity for light excitation above and below ca. 500 nm.

1. Introduction

The use of titania based photocatalysts has emerged as a powerful, advanced oxidation process to control environmental and health-related effects derived from chemical contaminants as well as from dangerous microorganisms. A main drawback of all titania based systems is their limited performance upon excitation at wavelengths above the UV limit of ca. 380 nm. This is a well known fact, intimately linked with the optical properties of the material and, particularly, with the relatively high band gap energy presented by all titania polymorphs, always above 3.0 eV [1–3].

Several technologies have been attempted to solve or mitigate this issue, being doping of the titania host a rather successful example. From the initial times of photocatalysis, doping was used to enhance performance under UV excitation. This objective leads to introduce Fe, Cu and other metals in relatively small quantities, below or around 1 at.% (cationic basis) [1–5]. Parallel to such development, effort was carry out with the aim of producing photoactive solids which can profit from a broad range of wavelengths in order to achieve a sunlight-operated catalyst. This was initially achieved mostly by decreasing the band gap of the titania and/or creating gap states with cationic [6–10], anionic [11–14] or cation-anionic co-doping [15–21]. These works concern the use of visible light photons as an additional energy source (to UV photons) of the photocatalytic process. More recently, the use of near IR photons captured the attention of researchers in the photocatalytic field. In this case, the source of the positive effect on photoactivity is under debate but at least originally the IR to UV upconversion process motivated a number of studies. Such works essayed the doping of titania mostly with Er but also co-doping with several rare earth always including Er as central doping cation of the solid catalyst [22–27]. Only few works focussed in the combination of what we can call visible light and near infrared light oriented cations. A representative example is the combination of Fe and Er [28].

Here we study the combination of previously tested and highly active photo-active materials concerning pure anatase powders doped with W (the visible light active cation [7]) or Er (the near IR active cation [22]). Note also that WO$_x$ species (called suboxides with W oxidation state below 6) at the surface of titania can also absorb IR photons trough a surface plasmon resonance [29,30]. These materials will be applied in the inactivation of microorganisms, specifically a Gram-negative (*Escherichia coli*) and a Gram-positive (*Staphylococcus aureus*) bacterium, that are known to cause hospital-acquired infections

because their resistance to most commonly used antibiotics. As well known, Matsunga and others provided the first reports of photocatalytic disinfection [31,32], opening a field subsequently flourishing with a large number of studies summarized in recent reviews [33–36]. Titania based catalysts are a kind of biocidal agent with significant advantages over conventional ones due, in first place, to the (relative) innocuousness of the material for humans, and, on second hand, to the absence of known weaknesses related to the type of organism, as the inactivation of Gram-positive and Gram-negative bacteria, viruses and fungi have been tested with significant success [1,33,37–41].

The work here presented attempts to understand the doping process of the single (Er, W) and codoped (ErW) systems by presenting an exhaustive study of the structural and electronic properties of the materials using x-ray diffraction, surface area measurements, UV–vis, photoluminescence, microscopy as well as x-ray photoelectron and absorption spectroscopies. The combination of techniques provides evidence that the codoping process renders powders with significant differences with respect to the single-doped materials. Such differences are reflected in the important efficiency offered by the codoped system in the photo-elimination of *E. coli* and *S. aureus* microorganisms. To interpret the catalytic results, a kinetic modeling was carried out following the work of Marugan et al. [42]. Modeling of the inactivation profiles is grounded in a simplified (Langmuir-Hinshelwood-like multistep-type) reaction mechanism and considers that microorganism death occurs via a sequential attack of photo-radicals by which "undamaged" cells become "damaged" and eventually progress to an "inactivated" state. The utilization of an "adsorption Langmuir-Hinshelwood" type mechanism allows a reasonable and relatively flexible description of the inactivation. Moreover, the advantage of using this approach appears two-fold: first, i) its usefulness for analyzing complete sets of inactivation profiles showing (or lacking) initial smooth/fast decays and final tailing section; and, additionally, ii) the model renders kinetic parameters allowing physical interpretation of the underlying process, in contraposition with many other simple kinetic laws [33,42,43]. Such work is combined with the electron paramagnetic and optical characterization of radical species formed under all illumination conditions relevant for this study. The combination of the structural and electronic characterization of the materials with the charge generation and kinetic analysis under light excitation provides evidence of the physical origin of the functional properties in our titania-based catalysts.

2. Experimental section

2.1. Catalysts preparation

Titania based materials were prepared using a microemulsion synthetic route and calcined at 723 K for 2 h as detailed previously in Ref. [44]. Briefly, titanium tetraisopropoxide was added to an inverse emulsion containing an aqueous solution (0.5 M) of ammonium tungsten oxide (Aldrich) and/or erbium nitrate (Aldrich) dispersed in n-heptane, using Triton X-100 (Aldrich) as surfactant and hexanol as cosurfactant. Water/titanium and water/surfactant molar ratios were, respectively, 18 and 110 for all samples. The resulting mixture was stirred for 24 h, centrifuged, decanted, rinsed with methanol and dried at 298 K for 12 h and subsequently calcined as mentioned. Samples were named Ti for the pure titania sample and W, Er or ErW for the doped materials. Cation content of calcined materials was measured by X-ray total reflection spectroscopy. Composition of the materials was adjusted considering the cation contents leading (according to literature) to optimum activity in the single-doped materials and the specific (visible or near IR) wavelength excitation [7,24].

2.2. Catalysts characterization

The BET surface areas and average pore sizes were measured by nitrogen physisorption (Micromeritics ASAP 2010). XRD profiles were obtained with a Seifert D-500 diffractometer using Ni-filtered Cu Kα radiation with a 0.02° step and fitted using the Von Dreele approach to the Le Bail method [45]; particle sizes and microstrain were measured with XRD using the Williamson-Hall formalism [46]. UV–vis diffuse reflectance spectroscopy experiments were performed with a Shimadzu UV2100 apparatus. Transmission electron microscopy (TEM) and X-ray energy dispersive spectra (XEDS) were recorded on a JEOL 2100F TEM/STEM microscope. XEDS analysis was performed with a probe size of ~5 nm using the INCA x-sight (Oxford Instruments) detector. Specimens were prepared by depositing particles of the samples to be investigated onto a copper grid supporting a perforated carbon film. Deposition was achieved by dipping the grid directly into the powder of the samples to avoid contact with any solvent.

XPS data were recorded on $4 \times 4\,mm^2$ pellets, 0.5 mm thick, prepared by slightly pressing the powered materials which were outgassed in the prechamber of the instrument at room temperature up to a pressure $< 2 \cdot 10^{-8}$ torr to remove chemisorbed water from their surfaces. The SPECS spectrometer main chamber, working at a pressure $< 10^{-9}$ torr, was equipped with a PHOIBOS 150 multichannel hemispherical electron analyser with a dual X-ray source working with Ag Kα ($h\nu$ = 1486.2 eV) at 120 W, 20 mA using C $1s$ as energy reference (284.6 eV). Surface chemical compositions were estimated from XP-spectra, by calculating the integral of each peak after subtraction of the "S-shaped" Shirley-type background, using the appropriate experimental sensitivity factors and the CASAXPS (version 2.3.15) software.

X-ray absorption spectroscopy measurements were carried out at BM26 beamline of the European Synchrotron Radiation Source (ESRF). Spectra at the W and Er L_{III}-edges were acquired using a Si(111) monochromator and Xe/N$_2$ filed ionization chambers. A He cryostat was utilized to obtain XAS (X-ray absorption spectroscopy) data from samples at 80 K. Energy calibration was achieved with the corresponding foils (W) or oxides (WO$_3$, Er$_2$O$_3$). Phase and amplitude functions were calculated using FEFF8.2 and experimental factors (S$_0{}^2$) derived from reference materials (WO$_3$ and Er$_2$O$_3$ oxides). Fitting results were obtained by using the VIPER program [47] and error bars were estimated with k^1/k^3 weighted fittings.

2.3. Analysis of radical species present after illumination

Electron paramagnetic resonance (EPR) measurements were carried out with a Bruker ER200D spectrometer operating in the X-band and calibrated with a DPPH standard. For the 5,5-dimethyl-1-pyrroline N-oxide (DMPO) spin trapping EPR experiments, the samples were suspended in water or methanol (at a concentration of $0.5\,g\,L^{-1}$) and were sonicated for 4 min. A solution (0.01 M) of DMPO spin trap (supplied by Sigma) was prepared and kept on ice during the whole set of experiments. Bidistilled water (Elix-10) or methanol (Sigma) were employed for these preparations. 100 μl of the solid suspension and 100 μl of the DMPO solution were mixed into an EPR flat quartz cell under atmospheric air and irradiated at different times, through a spectroscopic Pyrex glass filter with a cut-off at ca. 280 nm, with light excitation source identical to that employed for the photokilling tests and allowing "monochromatic" radiation (± 20 nm half width), being then immediately transferred to the spectrometer cavity for EPR analysis. A small radical concentration decay (of ca. 5% on average) was observed in the dark during the course of spectrum recording. The latter were obtained at 298 K at ca. 9.75 GHz microwave frequency, 19.5 mW microwave power, 100 kHz modulation frequency, 1 G modulation amplitude and 2×10^5 spectrometer gain. No significant signal saturation was observed in those conditions. Blank experiments were also performed over mixtures of 100 μl of the DMPO solution and 100 μL of water or methanol to check the absence of radical formation in the absence of solid under the employed conditions.

To measure peroxide radicals we carried out a reaction with acidified TiOSO$_4$ as thoroughly described in Ref. [48]. In short, hydrogen

peroxide reacts rapidly with Ti(IV) ions producing a peroxo complex with characteristic deep yellow color. The study of H_2O_2 formation under different illumination conditions was made by mixing 3 mL of catalyst´s suspension in water (1 mg/mL) with 3 mL of $TiOSO_4$ (280 mM). Then, the final solution was subsequently irradiated for different times, measuring the optical absorbance of the corresponding aliquot in a quartz cuvette at 410 nm and using the UV–vis spectrometer above described.

2.4. Microbiological tests

The microorganisms used in this study include *E. coli* 1337-H and *S. aureus* 1341-H and were obtained from the German Collection of Microorganisms and Cell Cultures (DSMZ, Braunschweig, Germany) and cultured and maintained according to the recommendations of the suppliers [49]. Briefly, *E. coli* 1337-H and *S. aureus* 1341-H were grown in Luria-Bertani (LB) medium at 37 °C using 100 mL flasks filled with 10 mL of the medium. As the physiological state of bacteria may influence the results, cells were grown until the exponential phase (OD_{600} 0.3) and subsequently used for photochemical cell viability assay [38]. Cells obtained under these conditions are fully viable, compared to those produced in stationary or late-stationary phase where viable cells may coexist with debris and dead cells. To study the antimicrobial activity of the powders, a suspension containing 10 μL of microbial cells (8.9 10^9 cell forming units (CFU) mL^{-1}) suspended in 1 mL broth solution was made [50]. Aliquots of 1 mL from these suspensions were added to a 4 mL quartz cubic cell containing 1 mL of sterilized water and the corresponding catalyst under continuous stirring and oxygen supply. The slurry (at a previously optimized concentration of 0.5 $g L^{-1}$) was placed in the UV spectrometer chamber (Synergy HT Multi-Mode Microplate Reader - BioTek) and irradiated with a light at 280 (UV), 425/500 (visible), 950/ 975 nm (near IR) for different time periods. The excitation linewidth is lower than 10 nm in all cases.

The samples together with blank tests (using either light without catalyst or the materials at dark conditions) were measured using the same bacterium inoculums (8.9 10^9 CFU mL^{-1}) for each microorganism tested. As demonstrated by blank experiments, care was put of using a sub-lethal, maximum radiation energy fluence of ca. 1 $kJ m^{-2}$ throughout the study. Excitation was carried with a UV–vis spectrometer (UVIKON 930) equipped with filters to obtain monochromatic radiation (± 10 nm half width). After irradiation and for different time intervals, aliquots of 100 μL were transferred to a 10 mL LB broth test tube. The order of cell dilution at this stage was 10^{-2}. Loss of viability after each exposure time was determined by the viable count procedure on LB agar plates after serial dilution (10^{-2} to 10^{-5}). All plates were incubated at 37 °C for 24 h after which they were scanned using a Bio-Rad Imaging System equipped with Analysis Software 4.6.5 (Bio-Rad) to enable enumeration of bacterial colonies among replicates. Detection limit of the automated method is below 10 colony units. Data reported in this contribution are the average of four to five different experiments.

2.5. Kinetic modeling

Modeling of the inactivation profiles was achieved, as mentioned, using an approach grounded in a simplified (Langmuir-Hinshelwood-like multistep-type) reaction mechanism based in three parameters; kinetic (k) and pseudo-adsorption (K) constants and an inhibition coefficient (n) [42]. The model considers that microorganism death occurs via a sequential attack of photo-radicals by which "undamaged" (denoted as u in subsequent equations) cells become "damaged" (denoted as d) and eventually progress to an "inactivated" state [33,42]. This leads to two differential equations as:

$$\frac{dN_u}{dt} = -k \frac{K N_u^n}{1 + K N_u^n + K N_d^n} \tag{1}$$

$$\frac{dN_d}{dt} = k \frac{K N_u^n - K N_d^n}{1 + K N_u^n + K N_d^n} \tag{2}$$

We modified this model by assuming a fast decay from "undamaged" to inactivated cells which would lead to a simplified mechanism with a single differential equation paralleling the one of a classical Langmuir-Hinshelwood mechanism:

$$\frac{dN_u}{dt} = -k \frac{K N_u^n}{1 + K N_u^n} \tag{3}$$

Numerical solution of the corresponding set of equations was achieved with a 5th order "adaptive size controlled" Runge-Kutta program, coupled to a Full Newton (non-linear fitting) algorithm in order to ensure the solution of the corresponding non-linear fitting problem [51]. Results reported here, e.g. in the specific reaction conditions used, concern the second model (single differential equation) as a better fit is obtained as judged by the coefficient of determination R^2. Note nonetheless the trends among the catalysts series using both models were the same, indicating that interpretation of the results are independent of the model.

3. Results and discussions

3.1. Physico-chemical properties

Table 1 collects results concerning the chemical composition of the samples. Tungsten was introduced in our powders in significant quantity, around 15 at. % (cationic basis). We doped the system with a relatively large quantity of tungsten as significant activity under both UV and visible illumination was observed for such large W concentration in a significant number of studies of titania based photocatalysts [5,7,8,52–54]. Erbium was close to 2 at.% in our samples, a quantity which can provide high activity under near-IR excitation [24,25,27]. For our series of samples the codoping decreases slightly (approximately 10%) the amount of alien cations with respect to the single-doped counterparts. We note that the chemical analysis of the samples did not detect N or other residues, coming from the metal precursors, above a 0.1 at. % concentration.

The XRD patterns of the catalysts are presented in Fig. 1. All samples display the anatase pattern (*JCPDS* card 78-2486, corresponding to the *I41/amd* space group). Some differences are however observed in the plot. They mostly concern the width of the peaks indicating differences in the crystallinity of the materials. Analysis of the primary particle size of the crystallites is presented in Table 1. As can be seen, our titania and Er-doped samples show the larger dimensions, ca. 13 and 11 nm, respectively. The presence of tungsten decrease of primary particle size significantly as reported earlier [5,19]. Both the single W- and codoped ErW powders show a diminished primary (crystallite) size with respect to the other samples of this study. The BET surface area displays a trend correlated with the above mentioned modification of the anatase primary particle size of the sample. Higher surface areas are connected with lower primary particle size, with a minor effect of erbium in both observables and a clear effect of tungsten with a decrease of primary particle size of at least 2 nm and an increase of surface area of ca.

Table 1
Main physico-chemical properties of the samples.[a]

Sample	TXRF/mol %		BET/$m^2 g^{-1}$	Size/nm	Band gap/eV
	Er	W			
Ti	–	–	77.5	13.1	3.04
WTi	–	14.9	115.0	8.8	2.96
ErTi	1.9	–	76.3	10.7	3.05
ErWTi	1.5	13.1	112.9	8.9	2.99

[a] Standard error: TXRD; 7%; BET 2 $m^2 g^{-1}$; size; 9.5%; bad gap; 0.03 eV.

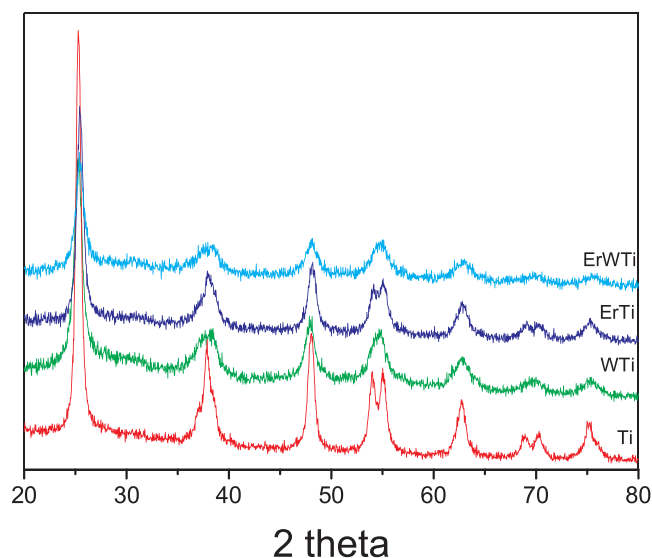**Fig. 1.** XRD patterns of the samples.

$30 \, m^2 \, g^{-1}$.

To progress in the structural study of the systems, we performed X-ray absorption experiments at the W and Er L_{III}-edges. The W L_{III}-edge results are presented in Fig. 2. The XANES spectra of the single and codoped powders display a while line intensity (characteristic of the

s → d transition) larger than a monoclinic WO_3 reference obtained using the same preparation procedure. This was previously observed in the single doped anatase-based material [55]. The edge positions (equal within experiments error among all tungsten containing materials) indicates a +6 oxidation state of tungsten in the solid, but with electronic alteration with respect to the corresponding tungsten single oxide. No differences are encountered between our W-containing samples indicating their similar properties in respect to tungsten electronic properties. As the Fourier Transforms of the EXAFS spectra displayed in Fig. 2 demonstrates, near identical spectra are obtained for our two tungsten-containing samples. This further corroborates the rather small (tungsten-related) differences between the single and codoped samples. The local structure of these two samples differs from the one of the WO_3 reference (the imaginary part of the Fourier transform indicates the different chemical nature of some neighboring atoms), particularly considering distances above the first W-O shell. In particular, in Fig. 2B the dashed lines at radial pseudo-distances near or above 2 Å show marked differences in W-O-M (M being a cation) links with respect to the WO_3 reference.

Quantitative analysis of the W L_{III}-edge EXAFS spectra provides further insights. Fitting results are summarized in Table 2 and are graphically displayed in Fig. 2 (dashed lines in panels C and D). The agreement between experimental and modelling spectra is indicative of the goodness of the fitting results. According to the Nyquist theorem, we have a number of free parameters (details included in Table 2) allowing the fitting of three shells [56]. These three shells correspond to two W-O bonding distances of ca. 1.78 and 2.66–2.67 Å, and a third W-
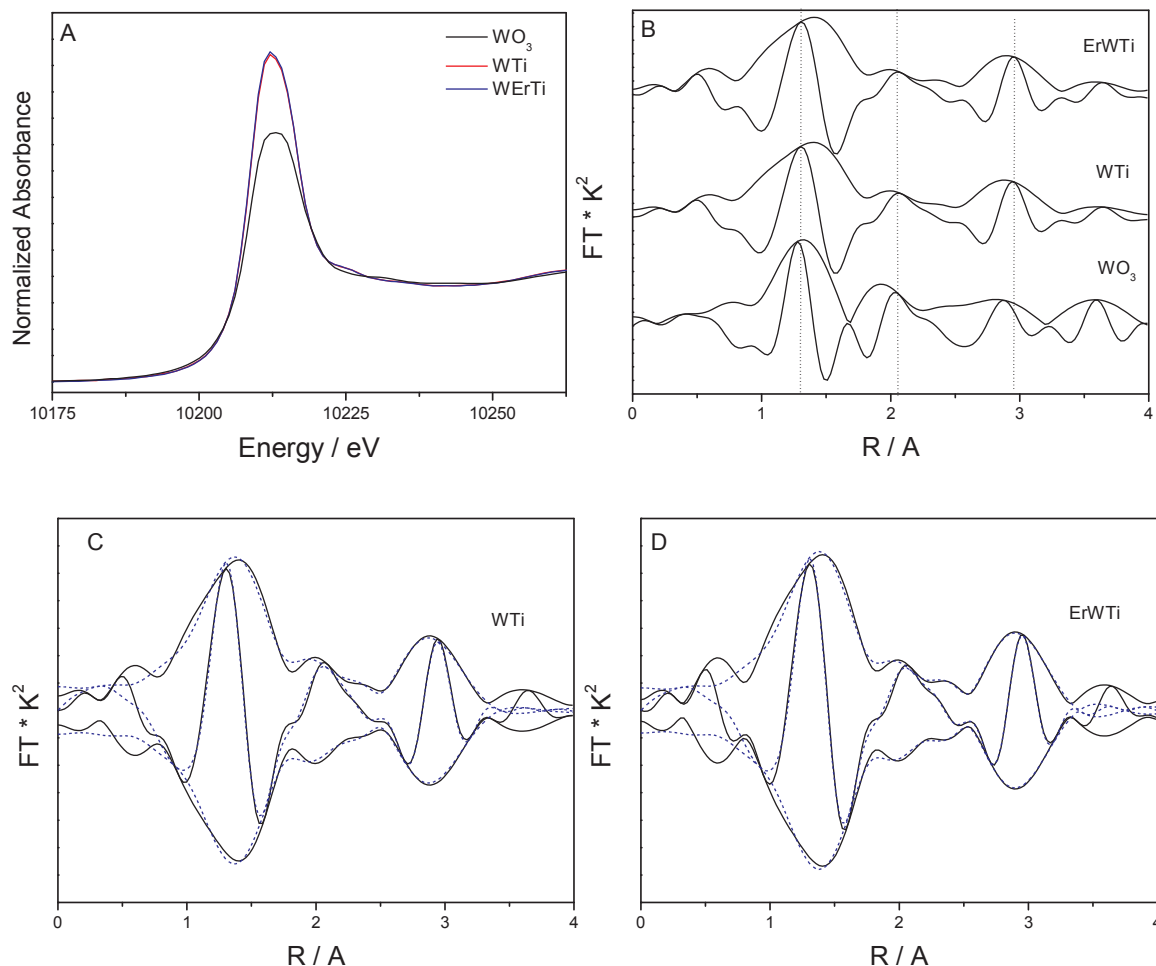

Fig. 2. XAS W L_3-edge results for the WO_3 reference, and W-containing single and codoped samples; a) XANES spectra; b) Fourier Transform module and imaginary part of the EXAFS spectra; c and d) Fourier Transform module and imaginary part of the EXAFS signal (full lines) and modelling results (dashed lines).

Table 2
Fitting results of the W L_{III}-edge EXAFS signals of the samples.[a]

Shell	R/Å	C.N.	$\Delta\sigma^2/Å^2$	$\Delta Eo/eV$
Sample: WTi				
W-O	1.78 ± 0.01	2.7 ± 0.3	0.0080 ± 0.003	1.1 ± 0.2
W-O	2.67 ± 0.02	3.2 ± 0.5	0.021 ± 0.009	8.3 ± 0.6
W-Ti	3.40 ± 0.01	3.5 ± 0.4	0.008 ± 0.002	−8.6 ± 0.7
Sample: ErWTi				
W-O	1.78 ± 0.01	2.5 ± 0.3	0.0085 ± 0.003	1.0 ± 0.2
W-O	2.66 ± 0.02	3.3 ± 0.4	0.021 ± 0.009	8.3 ± 0.6
W-Ti	3.40 ± 0.01	3.4 ± 0.4	0.00851 ± 0.002	−8.5 ± 0.7

[a] The fitting is carried out in k: 2.60–10.91 Å^{-1}; R 0.92–3.35 Å ranges; free parameters according to Nyquist theorem: 14.

Table 3
Fitting results of the Er L_{III}-edge EXAFS signals of the samples.[a]

Sample/Shell	R/Å	C.N.	$\Delta\sigma^2/Å^2$	$\Delta Eo/eV$
Sample: ErTi				
Er-O	2.18 ± 0.01	6.0 ± 0.5	0.0221 ± 0.006	−0.05 ± 0.1
Er-Ti	2.67 ± 0.02	3.8 + 0.4	0.0209 ± 0.007	7.2 ± 0.8
Er-Ti	3.48 ± 0.02	1.3 + 0.3	0.004 ± 0.001	9.4 ± 1.0
Sample: ErWTi				
Er-O	2.29 ± 0.02	6.3 ± 0.5	0.0015-0.005	4.3 ± 0.3
Er-W	3.11 ± 0.01	1.0 ± 0.2	0.0018	−8.0 ± 0.5

[a] The fitting is carried out in k: 3.09–9.26 Å^{-1}; R 0.88–3.64 Å ranges; free parameters according to Nyquist theorem: 12.

Ti at ca. 3.40 Å. The coordination numbers of the two W-O cells indicates the distortion of the octahedral local geometry of anatase in a 3 + 3 environment. Such environment is characteristic of the local order of W in tungsten oxides [57]. The third distance demonstrates the formation of a W-Ti substitutionally disorder mixed oxide, where tungsten occupies Ti positions. Such substitution produces Ti vacancies as anatase would have a Ti-Ti second coordination shell number of 4. W expands the characteristic first cation-cation distance (M-O-M shells) appearing in bare anatase at 3.05–3.10 Å [58], and reduces the coordination number in a quantity corresponding to a titanium cation vacancy for each 2 tungsten cations. Therefore, tungsten has (first neighboring) oxygen atoms in a local geometry resembling that of the pure tungsten oxide with monoclinic structure but within a (medium and) long range order corresponding to an anatase structure.

Corresponding X-ray absorption experiments at the Er L_{III}-edge are shown in Fig. 3. The same edge position of the tree XANES spectra (panel A) indicates a +3 oxidation state of Er, characteristic of the Er_2O_3 reference. As occurring in the W L_{III}-edge, our samples display larger white line intensity than the reference but in this case also showing differences among them. The codoped powder owns a more pronounced while line (dominated as mentioned by the p → d transition), indicative of a larger electronic modification in d electron count with respect to the single doped material and this in turn than the erbium oxide reference. The presence of erbium at the anatase structure alters this cation electronic structure with dependence of the chemical composition of the sample and particularly if tungsten is present or not. This is again inferred from the EXAFS Fourier Transform signals collected in Fig. 3B. It is particularly evident the different environment of the three samples around and above ca. 2.5 Å, indicating changes in
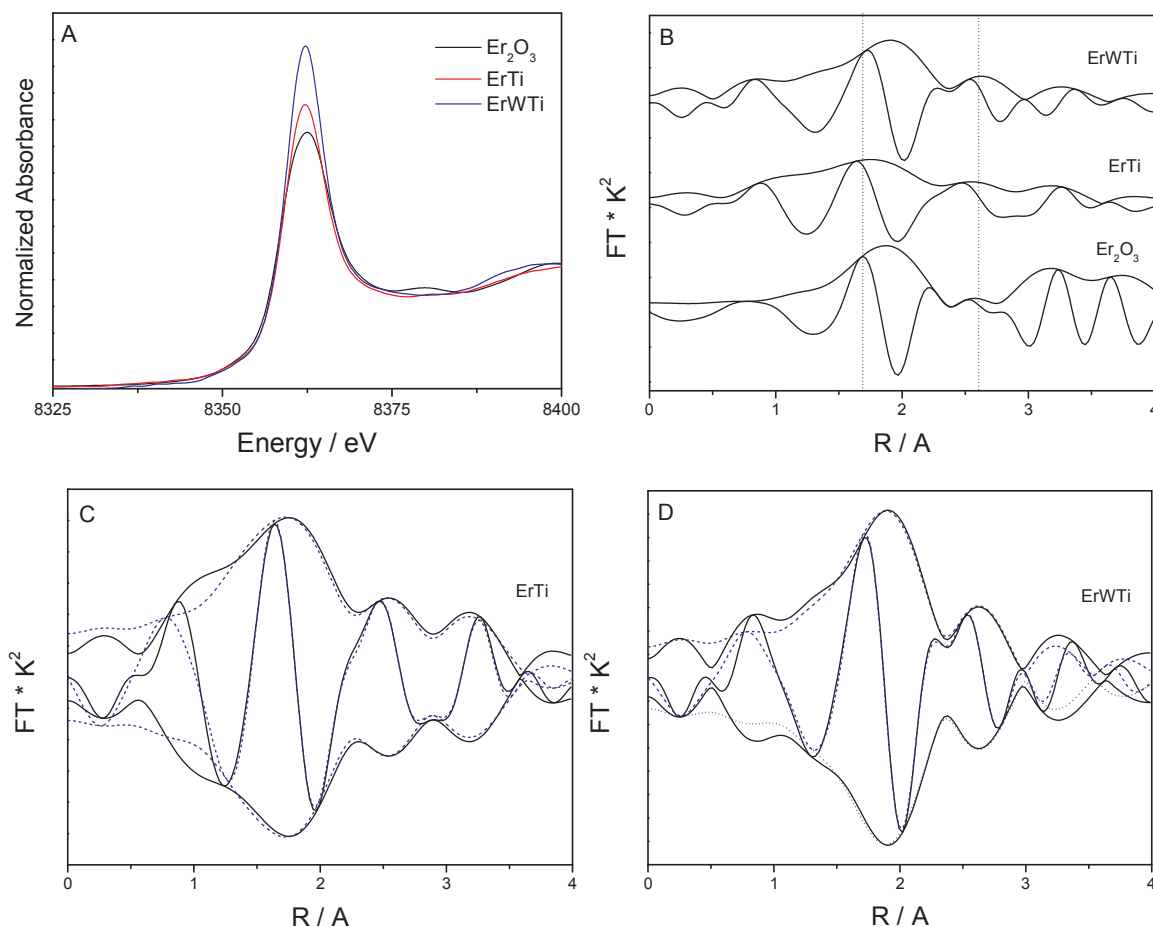

Fig. 3. XAS Er L_3-edge results for the Er_2O_3 reference and Er-containing single and codoped samples; a) XANES spectra; b) Fourier Transform module and imaginary part of the EXAFS spectra; c and d) Fourier Transform module and imaginary part of the EXAFS signal (full lines) and modelling results (dashed lines).
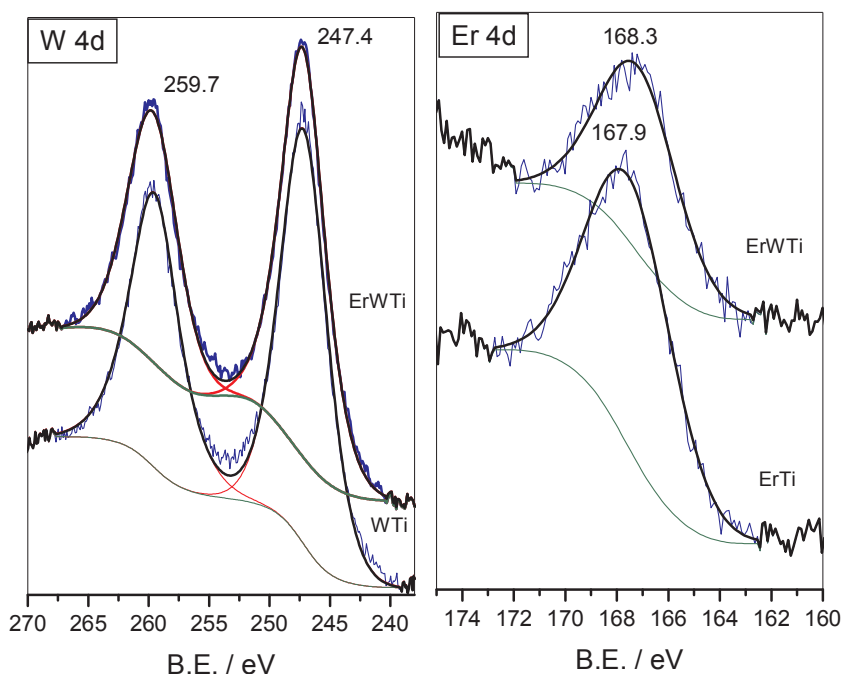
Fig. 4. W 4d and Er 4d XPS for the samples.

Table 4
XPS binding energy and atomic ratios. In parenthesis atomic ratios from TXRF.[a]

Sample	Ti 2p/eV	O 1s/eV	Er 4d/eV	W 4d/eV	O/(M + Ti)	W/Ti	Er/Ti
Ti	458.2	530.0	–	–	2.45	–	–
WTi	458.4	529.9	–	247.2	2.49	0.29 (0.18)	–
ErTi	458.2	529.6	167.9	–	2.63	–	0.013 (0.020)
ErWTi	458.4	529.8	168.3	247.3	2.54	0.23 (0.15)	0.009 (0.018)

[a] Standar error: Binding energy 0.1 eV; Atomic Ratios; 8.5%.

local environment.

The quantitative Er L_{III}-edge EXAFS fitting results are summarized in Table 3 and are graphically reported in Fig. 3 (dashed lines in panels C and D). The number of free parameters in the erbium case allows the use of a maximum of three shells (details at Table 3). In the single doped sample the fitting renders one Er-O at 2.18 Å and two Er-Ti shells at, respectively, 2.67 and 3.48 Å. The distance and corresponding co-ordination number (ca. 6.) of the Er-O shell are typical of the Er(III) oxide [59] but the next two coordination shells are strongly indicative that erbium is located at the anatase network in all cases (single and codoped samples). The erbium substitution at the cation sub-lattice of anatase generates, on the other hand, a strong distortion of the local environment around the alien cation. This is due to the large difference in ionic radius between Ti (0.605 nm in octahedral coordination) and Er (0.89 nm), contrarily to tungsten (0.60 nm) [60]. In this single doped sample, the distances of the two Er-Ti shells would be the result of a mixture of local environments present in the single Er and Ti oxides. The short first Er-Ti distance would indicate that a limited number of Ti cations would occupy interstitial positions near Er (as a consequence of the charge neutrality defects occurring at anatase in presence of the doping cation). Therefore, as occurring with tungsten, erbium has oxygen neighbours with a local symmetry resembling that of the pure oxide but within a (medium and) long range order of the anatase structure.

The presence of tungsten in the anatase structure makes a strong influence in the erbium local environment for the codoped sample. A first point is the increase (with respect to the single doped material) of the Er-O coordination distance up to 2.29 Å, followed by the presence of tungsten at ca. 3.11 Å. Titanium cations may be likely present around or above the last distance mentioned, however the fit goodness (according

to an F-test [56]) does not increase enough to be statistically significant if a third shell is included. The presence of tungsten is thus part of the distortion displayed by the erbium local structure with respect to the single Er-doped catalyst. It should be noted that erbium is not observed at the W local environment. This is primarily an effect of the different doping concentration; tungsten has a higher concentration than erbium by a factor of ca. 9. The corresponding W-Er shell would have thus a relatively low frequency and coordination number (the latter according to the Er-W one), being consequently not observed in the corresponding W L_{III}-edge due to the fact that X-ray absorption is a bulk-averaged technique.

In short, the XAS study of the two doping cations indicates that titanium, tungsten, and erbium are located at the anatase structure forming a substitutionally disordered mixed oxide. All cation atoms have a local structure with differences in the neighboring oxygen atoms but are essentially located at lattice positions of the anatase structure (which provides the long order range of the oxide) and display a first neighboring cation (M1-O-M2 distances) dominated by Ti, expect for the Er cation in the ErW sample.

X-ray photoelectron spectroscopy (XPS) was also utilized to characterize our samples and corresponding results are shown in Fig. 4. Specifically, Fig. 4 displays W4d and Er4d XPS spectra as well as fitting results. Parameters from the fitting of the XPS peaks are summarized in Table 4. Ti and O XPS peaks show positions corresponding to the Ti^{4+} oxide(s) [61]. W shows a single contribution with binding energy value corresponding to the +6 oxidation state, in agreement with the XANES study and previous results reported for substitutionally disordered W-Ti mixed oxides [7,8]. The Er_2O_3 oxide displays a Er 4d binding energy of 168.5 eV [61]. However, when such cations is located in or onto the
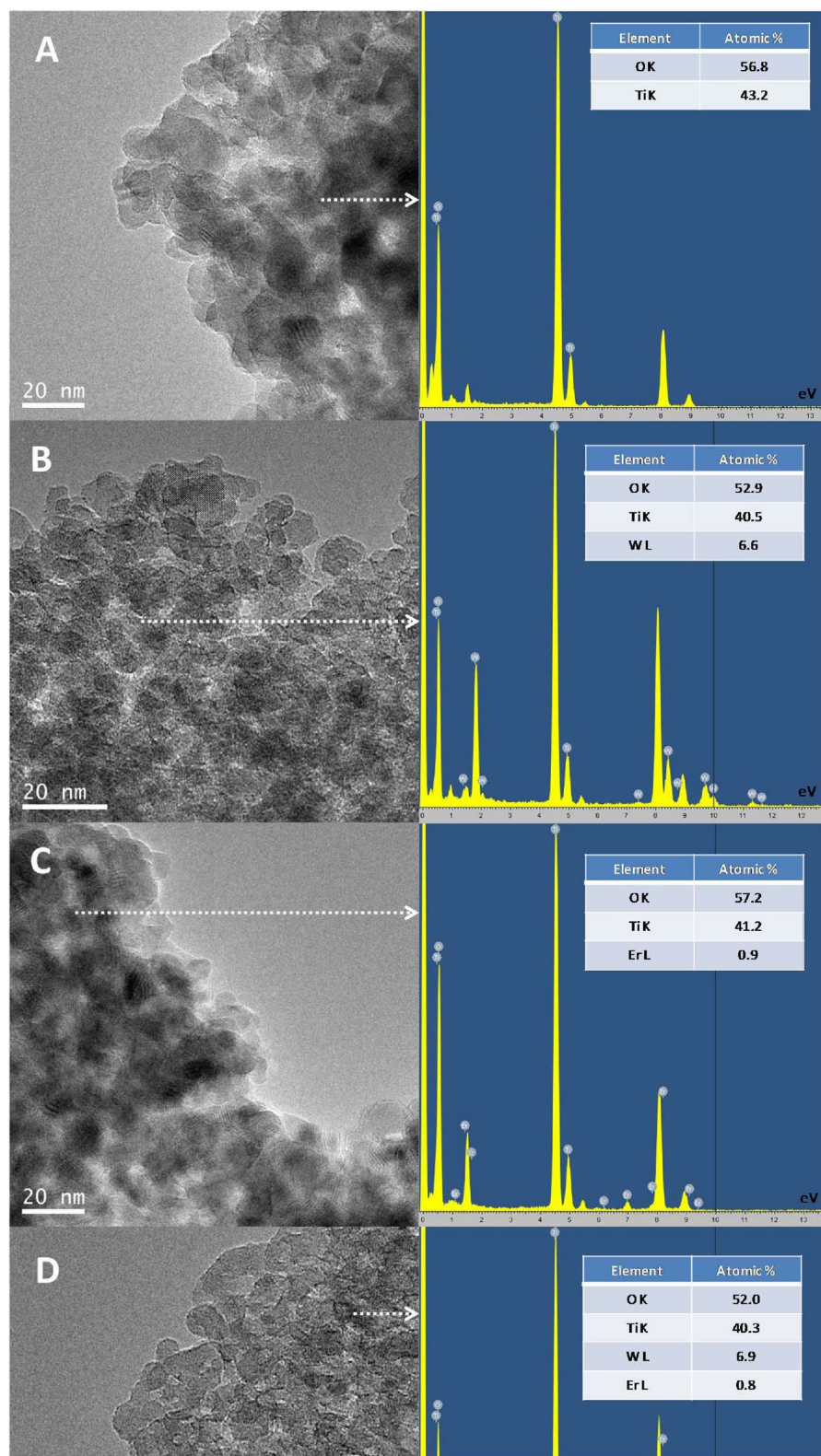
anatase structure, the solids display rather broad Er XPS peaks, with energy varying above or below the mentioned oxide reference characteristic energy position [24,25]. This indicates that important structural differences at the local structure around Er may be encountered as a function of the preparation method. This would be connected by differences in the erbium surface depletion or enrichment observed in the different works [24,25]. In our case, the preferential presence of erbium at bulk positions (with a characteristic local order) renders a lower binding energy than the one of the bare erbium oxide. Tungsten presence counteracts partially the situation increasing the binding energy of erbium. The different local environment of erbium in the single and codoped samples (Table 3) makes difficult to ascribe changes in the XPS binding energy to simple electronic differences. In fact, the XPS binding energy must reflect differences between the single and codoped
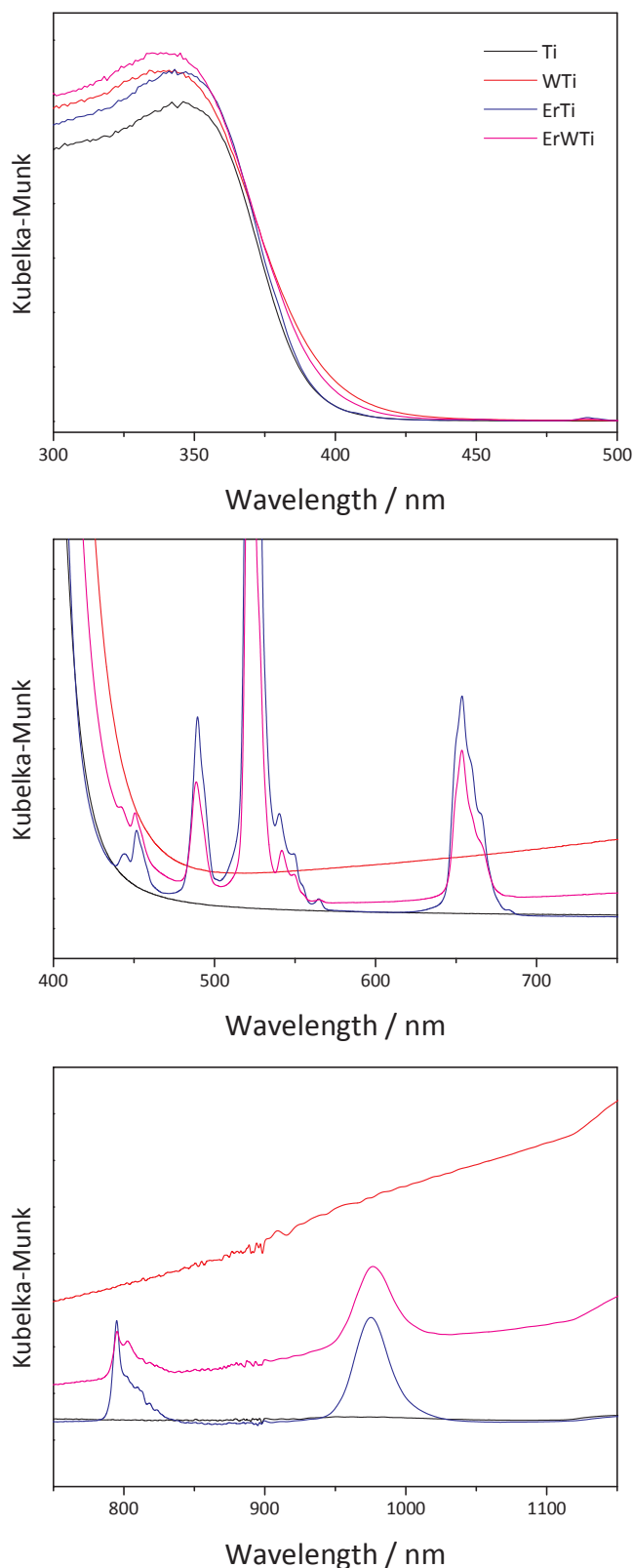
Fig. 6. UV–vis spectra of the samples. Upper panel: zoom view in the UV and near-visible region; medium panel: zoom view centered at the visible zone; lower panel: zoom view centered at the near IR zone.

samples concerning the Er–O bond (occurring at distances differing ca. 0.1 Å) and the modification of the chemical nature of the neighboring cations from Ti to W.

We further analyze the solid with the help of microscopy. Fig. 5

displays TEM micrographs showing anatase platelets with typical dimension in the 10 nm range (in agreement with XRD) and showing relatively limited variations among the samples and, particularly, with respect to the bare titania reference. Absence of significant differences in the anatase crystallites were observed using high resolution (result not shown). The XEDS analysis, also presented in Fig. 5, showed the presence of the doping cations in the corresponding samples. Although with some variation (going from 0.3 to 2.8 at.% for Er and 7.1–17.5 at. % W; expressed in cation basis), we detected the doping cations (ca. 25 analyses per sample) in all XEDS analyses, indicating a reasonable dispersion of both cations throughout the whole catalyst(s).

From the structural analysis we see that the formation of a (W and/ or Er containing) substitutionally disorder anatase oxide structure occurred in all samples, where all cations occupy Ti sub-lattice positions of the network. Differences among samples are exclusively related to the local order around cations, and particularly marked in the erbium local environment in going from single to codoped catalysts. Such difference does not exist in the case of tungsten. The microscopy study showed the presence of the doping cations in all (tested) crystallites of the anatase powders. From a XPS analysis of the surface (Table 4), we can conclude that the samples show limited variation in oxygen content as well as a moderate tendency to present tungsten at the surface and erbium at the bulk. Both points are maintained in single and codoped samples with some (relatively minor) differences. Presence of tungsten alters morphology (primary particle size and surface area) to an important degree while erbium does not, likely by its preferential bulk position and lower concentration.

From an electronic point of view, tungsten displays a +6 oxidation state in the anatase structure and does not suffer alternation in presence or absence of erbium. Erbium has a dominant +3 chemical state but changes in the d count are obvious in presence or absence of tungsten. The codoping generates a substantial electronic modification of the erbium cation with respect to the single doped and the erbium oxide references. From a photocatalytic view, as important as the electronic behaviour of the oxides are the optical properties. To check it, we combined UV–vis and Photoluminescence spectroscopies.

The UV–vis spectra of the samples are collected in Fig. 5. The upper panel makes visible some differences in the region dominated by the band gap of anatase at ca. 380 nm [62]. The corresponding band gap, calculated considering anatase as an indirect gap semiconductor [63], are collected in Table 1. As observed previously in the literature, the band gap values indicate that tungsten moderately decreases the band gap energy of anatase while erbium does show a influence in this physical parameter [7,8,24,25,54]. This is primarily an effect of the doping concentration of our samples, as tungsten and erbium have been reported to produce a band gap red shift as a function of the concentration [8,54,64]. Codoping seems to counteract in a soft manner the effect of tungsten decreasing the red shift presented by the single doped powder.

Just after the UV–vis region dominated by the anatase band gap, the UV–vis spectra display a series of lines ascribed to the excitation of Er^{3+} species [65]. All these lines have structure (sublines) and display maxima at ca. 452, 490, 522, 654, 715 and 973 nm. They correspond to transitions from the Er^{3+} ground state $^4I_{15/2}$ to higher energy levels. Such transitions can induce electromagnetic effects beneficial for charge separation upon visible light excitation of the solids [66]. Intensity of such transitions suffers a mild reduction in presence of tungsten. In addition to such Er-related electronic transitions, Fig. 5 shows the effect of tungsten in the baseline of the corresponding spectra. This is an effect of limited magnitude in the visible region but is more evident close to the near IR region. This feature appears related to the presence of a broad range of (structurally different) defects and associated electronic states coming from tungsten suboxides present at near surface positions of anatase [29,30].

Photoluminescence spectra of the materials are collected in Fig. 6. They provide information related to the charge recombination taking
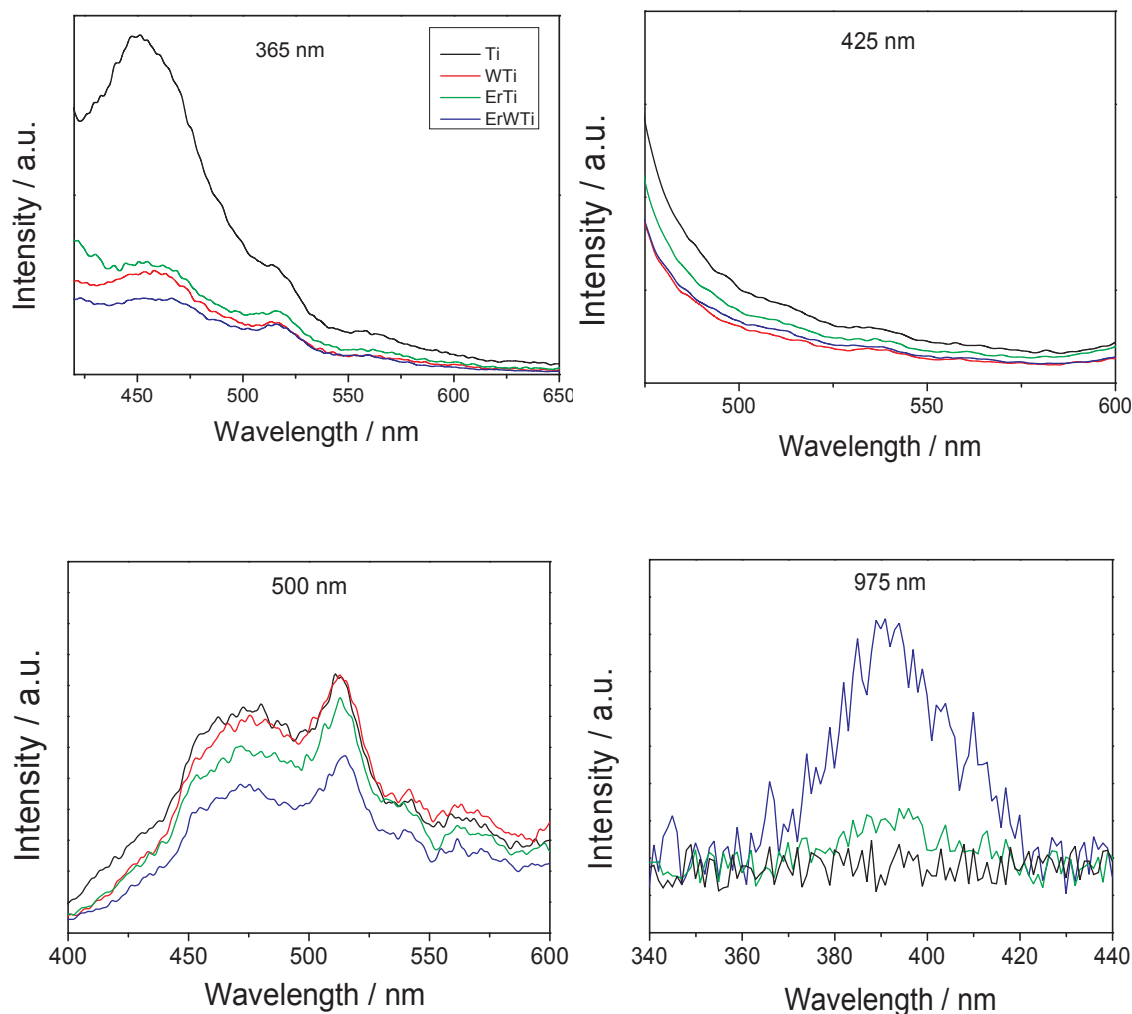
Fig. 7. Photoluminescence spectra of the samples. Each panel displays the excitation energy used.
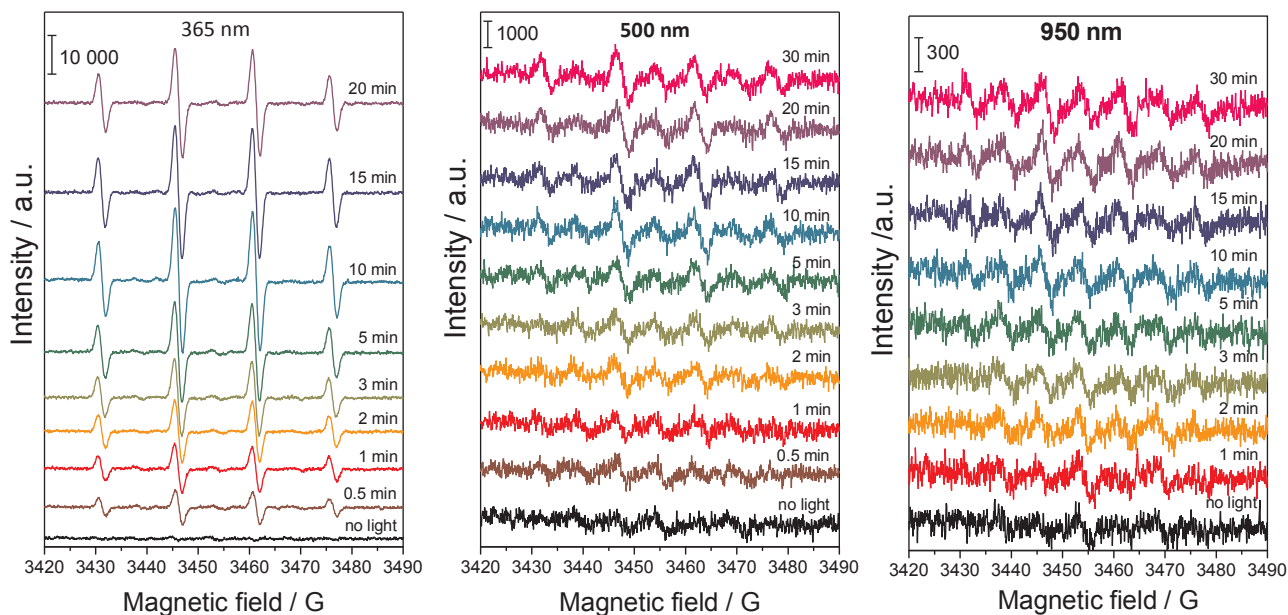

Fig. 8. EPR spectra obtained (365, 500 and 950 nm are used as representative examples) under illumination after different contact times in presence of the ErW-Ti sample dispersed in water.
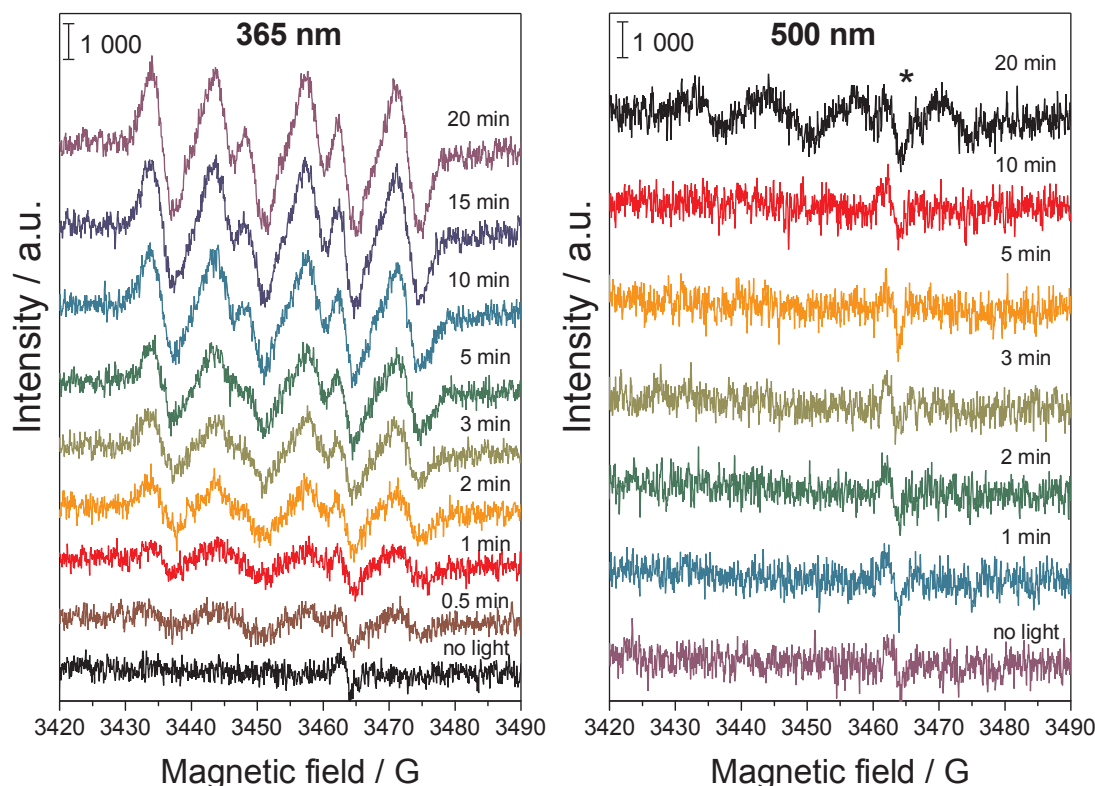
Fig. 9. EPR spectra obtained under illumination (365 and 500 nm are used as representative examples) after different contact times in presence of the ErW-Ti sample dispersed in methanol. The asterisk marks the cavity signal.

place after light excitation and thus render information of interest in photocatalytic processes [67,68]. Upon 365 nm excitation, we observed the typical decay curves of anatase materials corresponding to two types of contributions ascribable to the annihilation of conduction band free electrons with trapped holes and valence band free holes with trapped electrons [68]. Our samples display bands or shoulders at ca. 450, 525 and 560 nm and the doping process affects significantly the intensity. The photoluminescence intensity displayed of the samples after 425 and 500 nm excitation is significantly depleted with respect to the one presented by UV excited spectra. The spectra for 425 nm excitation are observed over a decay profile corresponding to the excitation line. In both cases (425 and 500 nm), rather minor and broad contributions corresponding to the de-excitation of localized electronic states can be observed. These are reasonably similar in all samples, indicating that the nanostructure is the main source of such behaviour. It appears in any case that the doping of titania produces a decrease of intensity which could be ascribed to a more efficient handling of the generated charge in the visible range. Note also that the photoluminescence spectroscopy is able to shown recombination of charge created after illumination for excitations going above the band gap energy (ca. 380 nm) up to ca. 500 nm. This demonstrates without doubt that localized electronic states are able to generate charged species under illumination.

Luminescence properties of erbium were also analysed using different wavelengths above 500 nm and only after excitation at 975 nm (Fig. 6) we observed the typical up-conversion emissions lines centred at ca. 385 and 410 nm and ascribable to near IR to UV–vis up-conversion [24,25]. The overall intensity seems to be enhanced in presence of tungsten.
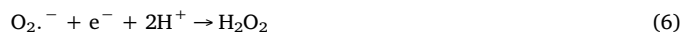
3.2. Radical species

In this work EPR and optical spectroscopies were used to characterize radical species. As well known, electron and holes produced after light absorption are transformed at the surface of the titania oxide to generate different types of radical species of interest in the photo-catalysis field. Main radical species of importance are considered hydroxyl-type, superoxide and hydrogen peroxide radicals [69,70]. There are other radical species such as singlet oxygen which can have importance in specific cases; however tests carried out here did not detect singlet oxygen radical species.

In the case of holes-related species, OH-type radicals are primarily formed following Eq. (4) [69,70].

$$H_2O + h^+ \rightarrow OH\cdot + H^+ \qquad (4)$$

Electrons capture in presence of oxygen gives rise to the superoxide radical (Eq. (5)) but such radical can evolve to produce a number of secondary molecules as described in Eqs. (6) and (7) [71–73].

$$O2 + e^- \rightarrow O_2\cdot^- \qquad (5)$$

$$O_2\cdot^- + e^- + 2H^+ \rightarrow H_2O_2 \qquad (6)$$

$$H_2O_2 + e^- \rightarrow OH\cdot + OH^- \qquad (7)$$

Note that Eq. (7) provides an alternative route to Eq. (4) for production of OH-type radicals. A fine analysis supporting the multi-step formation of the **OH·** type radical using different radical scavengers has been presented recently [74].

The study of all radical species formed in Eqs. (4)–(7) requires, as mentioned, a multitechnique approach. We first tracked hole-related species using EPR and probe molecules. Irradiation of DMPO-containing sample water suspensions gives rise to one dominant signal under UV (365 nm) and two different signals in the remaining cases analyzed. Fig. 8 displays the EPR experiment carried out for the ErW sample and selected wavelengths. The most prominent radical species detected corresponds to a signal with a 1:2:2:1 intensity pattern. Its EPR parameters (g = 2.0056, a_N = 14.9 G, a_H = 14.9 G) are characteristic of DMPO-OH adducts generated by the reaction of the probe molecule and
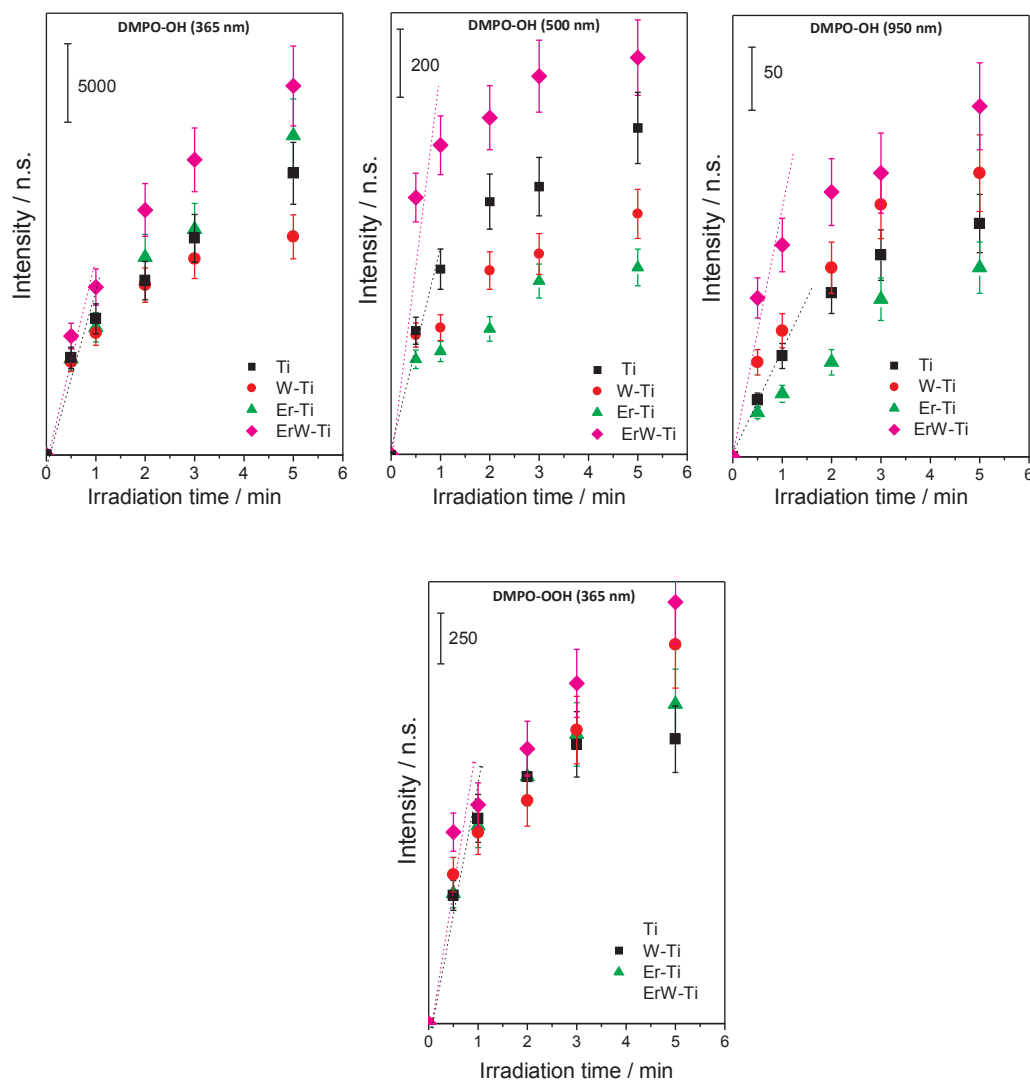
Fig. 10. Evolution of the radical species signal intensity for the experiments presented in Figs. 8 and 9 as a function of irradiation time using 365, 500 and 950 nm excitation wavelengths. Lines correspond to the initial slope for the rate of radical(s) formation for Ti and ErW-Ti samples.

Table 5
Values of initial rates of radical formation ($r_{OH^\bullet}$, $r_{OOH^\bullet}$, $r_{H_2O_2}$) for the samples. The number of species corresponds to number of spins ($r_{OH^\bullet}$ and, $r_{OOH^\bullet}$) or micromoles (H_2O_2).

$r\left[\frac{Number\ of\ species)}{min}\right]$	Wavelength/nm			
	365	425	500	950
SAmple Ti				
OH$^\bullet$	11,270 ± 1690	1223 ± 225	605 ± 130	85 ± 29
OOH$^\bullet$	1340 ± 295	n.d.[a]	n.d.[a]	n.d.[a]
H$_2$O$_2$	3.3 ± 1.4	n.d.[a]	n.d.[a]	n.d.[a]
Sample W-Ti				
OH$^\bullet$	10,680 ± 1520	1154 ± 220	479 ± 105	124 ± 42
OOH$^\bullet$	1240 ± 265	n.d.[a]	n.d.[a]	n.d.[a]
H$_2$O$_2$	_[b]	_[b]	_[b]	_[b]
Sample Er-W				
OH$^\bullet$	11,190 ± 1700	1098 ± 220	415 ± 110	53 ± 18
OOH$^\bullet$	1330 ± 285	n.d.[a]	n.d.[a]	n.d.[a]
H$_2$O$_2$	_[b]	_[b]	_[b]	_[b]
Sample ErW-Ti				
OH$^\bullet$	13,395 ± 2010	2156 ± 430	1127 ± 235	195 ± 53
OOH$^\bullet$	1610 ± 335			
H$_2$O$_2$	4.1 ± 1.9	n.d.[a]	n.d.[a]	n.d.[a]

[a] N.d. no detectable (below detection limit).
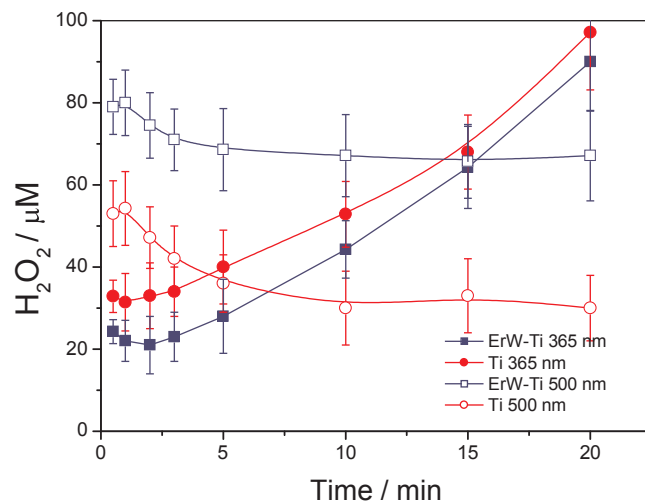[b] Not measured.

Fig. 11. Time evolution of the H$_2$O$_2$ species for different excitation wavelengths (365 and 500 nm).

hole related species [75,76]. The accumulation of DMPO-OH radical adducts grows continuously in all cases but such radicals have a limited stability and a maximum concentration as a function of time is always detected. The latter is an effect of multiple additions, within
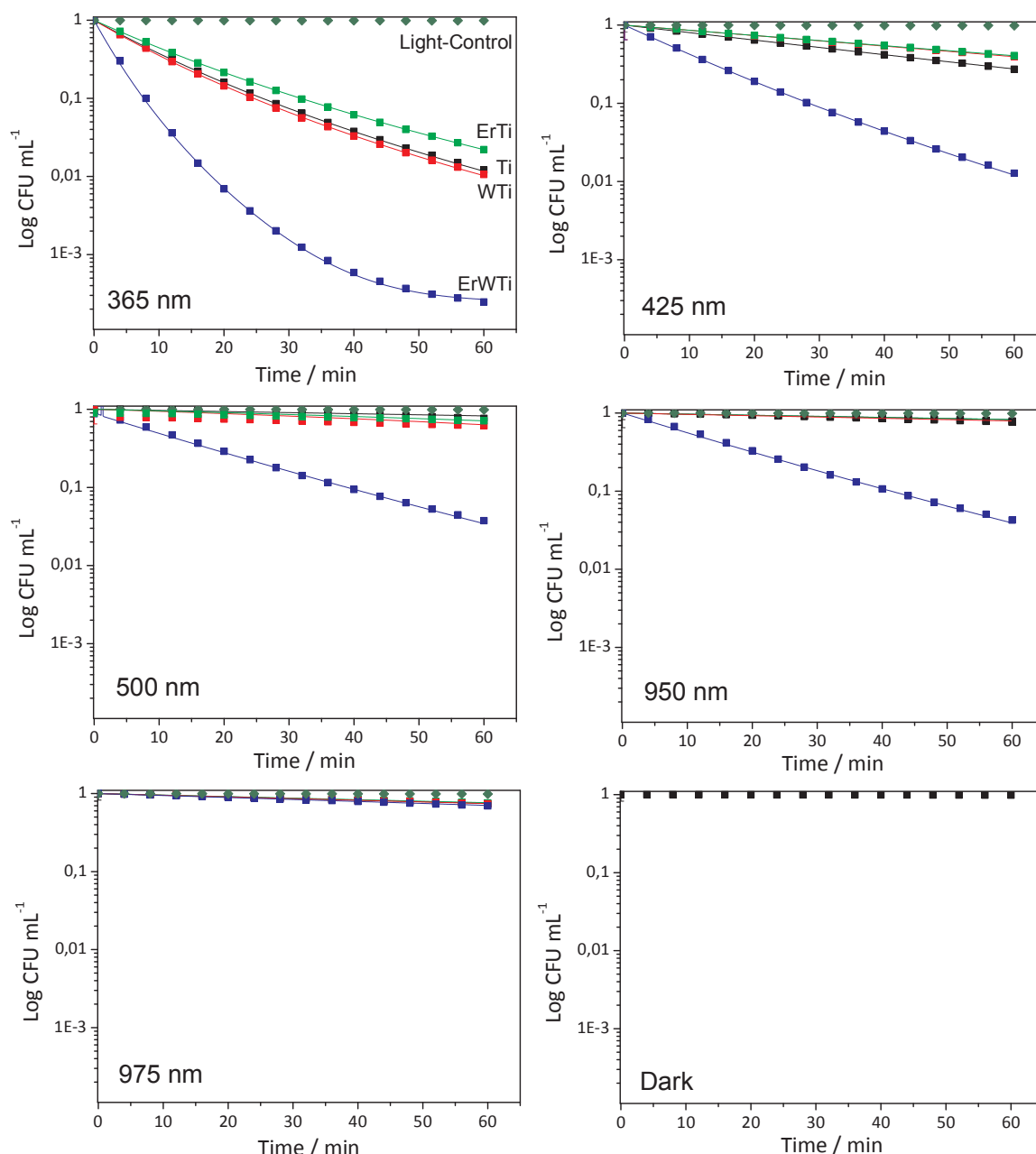
Fig. 12. Time of course of the *E.coli* inactivation under different excitation energies (365, 425, 500, 950 and 975 nm): ■ Ti ■ ErTi ■ ErW ■ ErWTi and ■ Light-Control experiments in absence of catalyst (only light). The last panel displays control measurements in absence of light (at dark conditions) using catalysts.

consecutive reactions, of OH radicals to DMPO molecules to yield diamagnetic species [75–79]. The second signal observed for all cases expect under UV illumination has an odd number of peaks and is most likely indicative of an interaction of the unpaired electron with a hydrogen nucleus (Fig. 8). The DMPO-H adduct shows a 1:1:2:1:1:2:1:1 intensity pattern with EPR parameters as follows: g = 2.0057, a_N = 16.6 G, a_H = 22.5 G [80,81]. The experiments carried out using methanol as solvent are presented in Fig. 9. Such experiments provide evidence of the formation of the DMPO-OOH adduct created by interaction of the probe molecule and the superoxide radical ($O_2^{\cdot-}$; radical which is easily protonated in water, rendering HO_2) and having EPR parameters such as g = 2.0056, a_N = 13.1 G, a_H = 12.1 G [81,82]. Such radical species is neatly observed under 365 nm illumination but is weakly observed up to 500 nm, being not detected under excitation with higher wavelengths.

As mentioned previously, due to the interaction of the spin probe

with multiple radical species along the time, a safe comparison of results under the different illumination conditions should be carried out on the basis of the radical species initial formation rate. Fig. 10 displays the intensity evolution with time for the different EPR-active radical species and Table 5 reports the numerical values of the initial formation rates as measured by the corresponding slopes displayed as dashed lines in Fig. 10. This figure shows the behavior of the different adduct species detected with EPR and only for illumination wavelengths where the radical formation rate is above the detection limit. While the DMPO-OH and DMPO-OOH adducts grow with time, indicative of their formation and evolution under illumination, the DMPO-H adduct (see Fig. 8) is formed immediately after illumination and essentially does not evolve. This fact indicates that the last adduct is not likely directly related to the photoactivity of the samples, as previously observed by others [75–79].

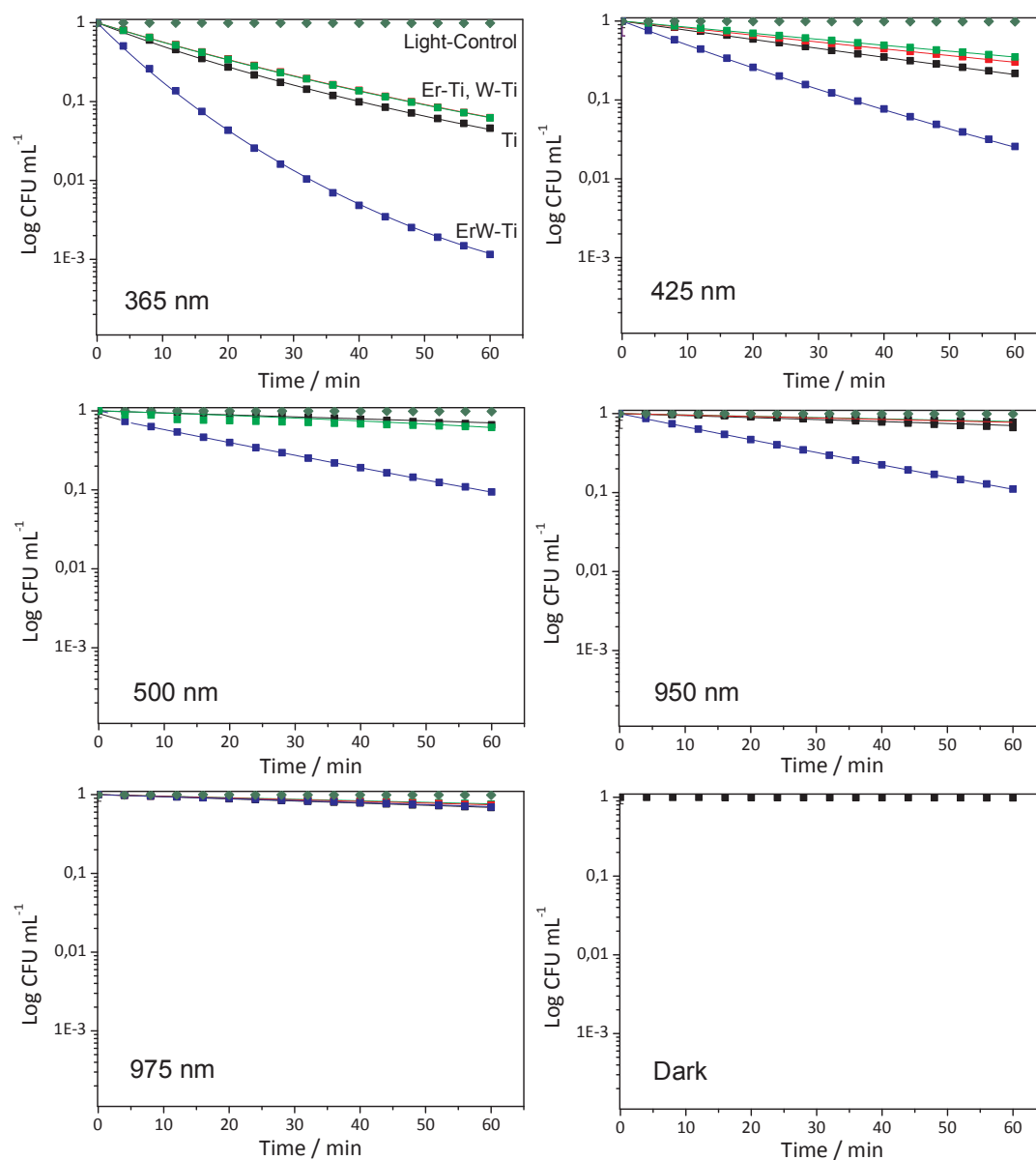Fig. 11 includes data concerning the formation of the H_2O_2 radical

Fig. 13. Time of course of the *S. aureus* inactivation under different excitation energies (365, 425, 500, 950 and 975 nm): ■ Ti ■ ErTi ■ ErW ■ ErWTi and ■ Light-Control experiments in absence of catalyst (only light). The last panel displays control measurements in absence of light (at dark conditions) using catalysts.

detected using optical tools. Under all illumination conditions we obtained minute concentrations of the radical. Only under UV illumination we can see a very mild increase of the radical formation with time, taking place after an induction period of a few minutes. The rather minute quantities measured and their evolution with time (without apparent correlation with the excitation energy or sample) indicate that the production of this radical species has no significance to justify photoactivity. In fact, significantly higher quantities of the H_2O_2 radical were detected for cases where it has relevance in the photocatalytic process [48].

Table 5 provides solid foundation for the analysis of the radical species formation. Moreover, the study of the radical species summarized in this table allows a quantitative comparison among samples and radical species. Inspection of Table 5 together with the previous discussion indicates that hydroxyl-type radicals are the reactive surface species dominantly formed. Besides it, we observe a moderate production of superoxide radical species and, as mentioned, an essentially negligible production of hydrogen peroxide. Comparing samples, we can say that the ErW-codoped sample shows a larger rate of radical

formation (independently of the specific radical species analyzed) than the other samples. Irrespective of the radical species analyzed, the bare titania and the single doped samples display limited differences, being Er the sample usually giving the lowest rate for radical species formation.

Data of Table 5 also informs about the evolution of the radical species formation rate with the light excitation wavelength. A strong reduction of the radical formation rate(s) occurs from 365 nm to 425 nm, irrespective of the sample. This issue points out a different source of the charge species. As documented by the optical (UV–vis and photoluminescence) characterization, the 365 nm excitation allows band gap excitation and creation of electron hole pairs. Above 380 nm (i.e. a band gap of ca. 3.0 eV) the excitation of charge involving (initial or final) localized states is the only possible mechanism. This may generate, depending on the excitation energy and catalyst structural properties, electron-hole pairs or hot-electrons in our samples [2,4,29,30,67,68].
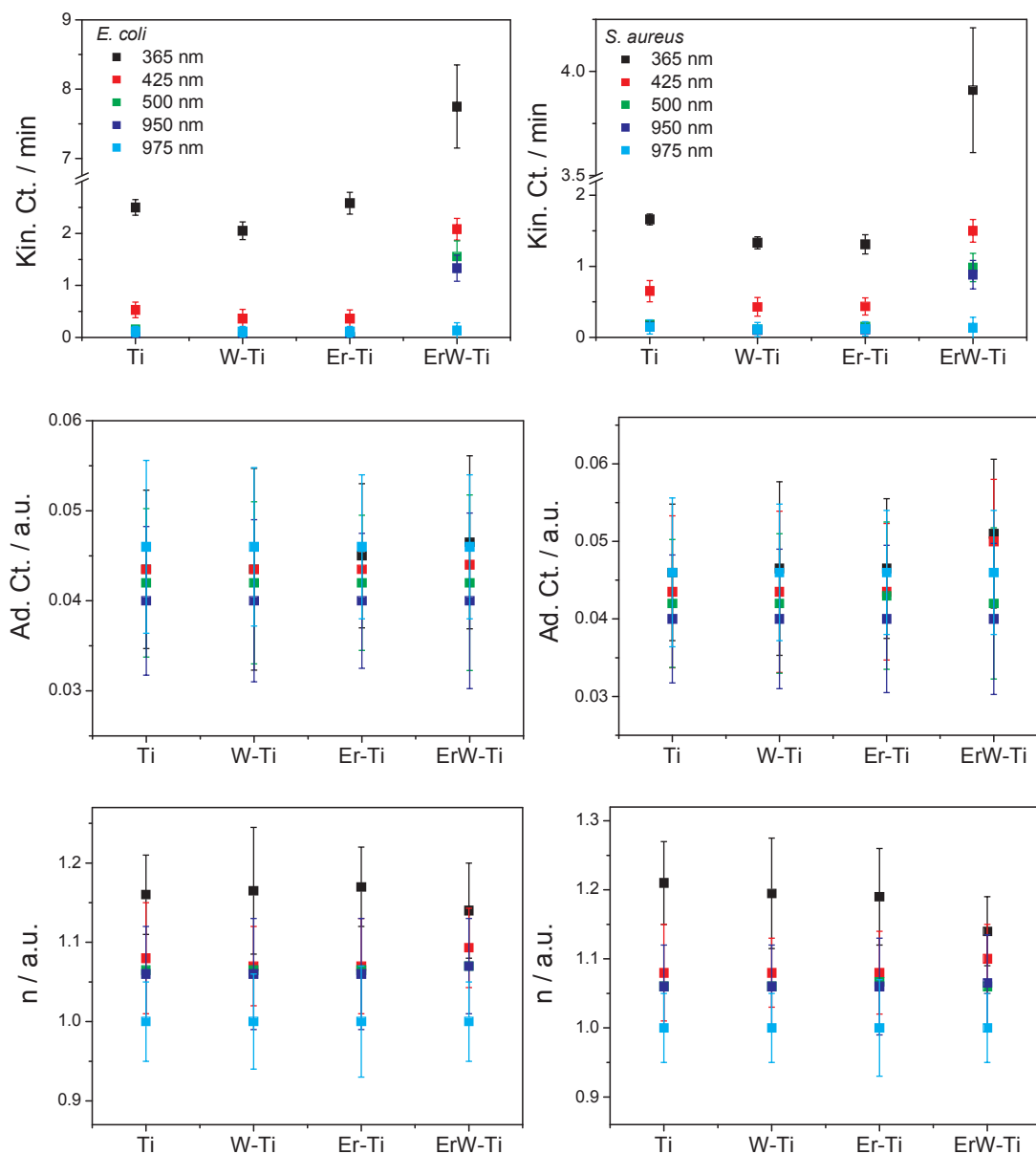
Fig. 14. Kinetic constant (upper panels), adsorption constant (medium panels), and inactivation coefficient (lower panels) for *E.coli* and *S.aureus* disinfection experiments presented in Figs. 12 and 13. Note the break in OY scale for the plots concerning the kinetic constants.

3.3. Photocatalytic activity

Figs. 12 and 13 report the result of the disinfection tests carried out using *E. coli* and *S. aureus* bacteria. Blank experiments without catalyst (s) are included in the figures and indicate the limited effect of the UV light (alone) in cell viability during the experiment. This is a direct consequence of the relatively low light intensity used in the experiment in order to maximize information [83]. Control experiments at dark conditions are included in a separate panel (last panel of the figure); catalysts do not show activity in such conditions. As a general rule for both microorganisms, the biocidal activity decreases as an inverse function of the wavelength. Note however that the solids can display activity in an important range of wavelengths measured but clearly with dependence of the chemical composition. In fact the (W and Er) single doped materials show minor differences with respect to the bare nanosized titania reference while the codoped system show enhanced activity in all conditions tested. Under UV activity is significant for all samples. The ErW-containing material renders disinfection activity at wavelengths near or above 500 nm, where the rest of systems

essentially lost their biocidal capability. The codoped powder maintains activity up to 950 nm.

Comparison of Figs. 12 and 13 shows that *E. coli* seems more sensitive than *S. aureus* to the biocidal action of all the photocatalytic powders here utilized. This is customarily discussed in the literature in terms of the membrane properties of Gram-positive vs Gram-negative bacteria [32–34], although the significance of this point in the biocidal action of titania systems is still under discussion [84–86]. Solid chemical composition was tested after the inactivation tests, showing absence of differences in all cases within experimental error. So, significant leaching of the cations to the liquid media is discarded.

As described in the introduction, here we utilized a "Langmuir-Hinshelwood" type mechanism as a reasonable and relatively flexible tool to describe the inactivation profiles displayed in Figs. 12 and 13 for the two microorganisms. Our approach is obviously a simplification of the real kinetics. Still the model allows us to qualitatively differentiate between the relative importance of the initial adhesion of the microorganism to the solid surface and the subsequent radical attack processes. The fitting results of the model are presented as full lines in
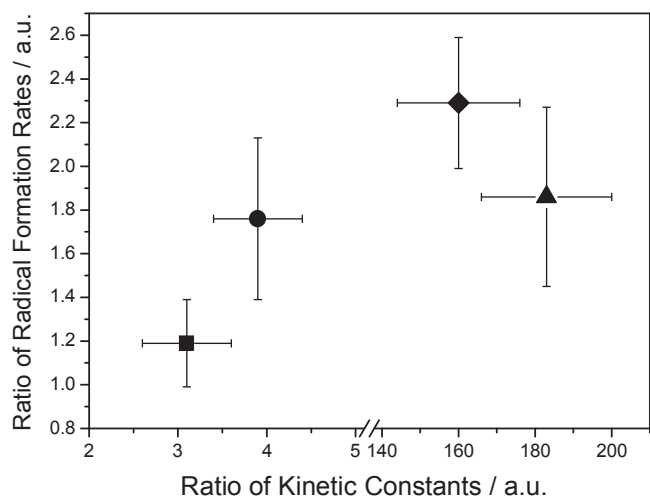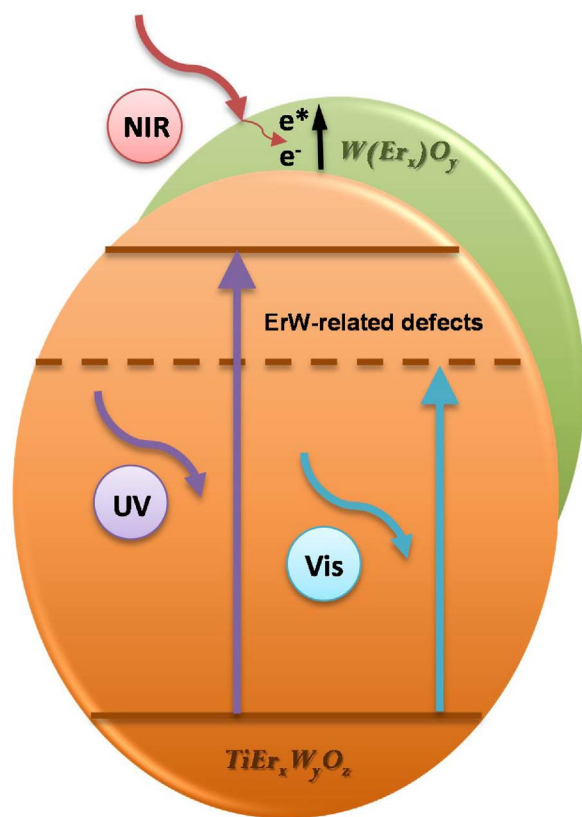
Fig. 15. Correlation plot between enhancement factors kinetic constant of *E. coli* elimination and radical formation rate measured with EPR. For all observables we plot as enhancement factor the ratio between values corresponding to the ErW-Ti vs. the Ti sample. Squares; 365 nm; circles 425 nm; triangles; 500 nm; diamonds; 950 nm. Note the break in the OX scale.

Scheme 1. Main light absorption events occurring in Sn-Ti samples.

Figs. 12 and 13. The presence of initial, slow inactivation profiles is followed in the most active cases by final tailing regions The adequacy of the kinetic model could be judged by the close description of the experimental results (including all initial and final regions of the curves), with rather high values, above 0.999 in all cases, of the coefficient of determination R^2.

The results of the kinetic analysis are presented in Fig. 14 for the two microorganisms, *E. coli* and *S. aureus*. As can be seen, major differences are encountered in the kinetic constant while the adsorption constant and inactivation coefficient display significantly lower variations among the samples of the series studied. For each microorganism, the values reported for the adsorption constant for all excitation wavelengths tested are equal throughout the sample series within experimental error. Slightly higher values are nevertheless presented for *S. aureus* with respect to *E. coli*. This indicates that the interaction of the microorganism with the solids (adhesion) is not severely modified in the single and codoped materials with respect to the bare reference system(s). Similarly, the inactivation coefficient values present reasonable similitude among samples (no differences within experimental error) but they do show a decreasing trend with excitation wavelength. The coefficient accounts for the inhibition produced by the increasing concentration of cell debris and oxidation products appearing toward the end of the experiment and competing strongly for the radical species effectively eliminating microorganism [42,43]. The inactivation coefficient is always higher than 1 and the higher the difference with the unity value the most important is the inactivation. The result for both microorganisms is the absence of important differences among samples. Differences in the coefficient behavior vs. the excitation wavelength (Fig. 14) parallel the decreasing biocidal power of the materials shown in Figs. 12 and 13; self-poisoned effects exerted by cell debris generated in the inactivation process are obviously proportional to the activity level. Still differences are small and only significant (out of the experimental error) when comparing wavelengths located at the two ends of the range studied, 365–975 nm.

The kinetic analysis is thus strongly indicative that differences in the disinfection capability of the samples can be described primarily as differences in the kinetic constant of the process and thus on the active centers of the disinfection process. Although the interaction of the microorganisms and the photo-oxide (the so-called adsorption process in our model) has been shown of significance in the photo-killing process [1,87,88], the kinetic analysis provides conclusive evidence that there is not a significant differential effect to justify the important activity enhancement shown by the ErW-codoped sample with respect to the bare titania oxide (Fig. 14). On the other hand, it is important to note that the two microorganisms here tested presented similar patterns in terms of photo-elimination evolution through the sample series and excitation wavelength (Figs. 12 and 13). We can thus concentrate in analyzing the properties of the solid active centers throughout the samples and as a function of the wavelength.

Tungsten decreases the anatase band gap to allow profiting from visible photons near the UV region, below ca. 425 nm (Table 1). However this is not reflected in a clear enhancement of the photo-elimination capability of the W-doped sample for the two microorganisms tested upon UV and near UV excitations (Figs. 12 and 13). Below ca. 500 nm we can observe a decrease in the photoluminescence intensity (Fig. 7; 365 and 425 nm excitations) for the ErW sample with respect to the titania reference and the two single-doped samples. This indicates a unique electronic behavior which can be correlated with the unique structural properties of the ErW sample demonstrated by XAS. When we plot the hydroxyl radical species rate of formation versus the kinetic constant in Fig. 15 (in both cases measured as the ratio between the ErW catalyst and the TiO_2 reference), a neat proportionality between the two observables is observed below 500 nm. The joint consideration of all these facts indicates that a more efficient charge carrier handling is reflected in a more efficient generation of hydroxyl-type radicals and microorganism inactivation.

With illumination above or near 500 nm the situation changes (Fig. 15). Titania and our single doped samples do not show activity if excited near or above 500 nm (Figs. 12 and 13). This is commonly observed in the literature [7,8,24–28,89]. Figs. 13–15 shows that ErW activity is not correlated with the generation of charge species. To interpret this result, we also note that photoluminescence experiments showed no significant up-conversion effect (Fig. 7). So, an explanation can be based in the plasmonic effect of the Er-W surface species present in the material [29,30]. Photoluminesce also shows that such effects decreases charge recombination and, more importantly, can generate

hot electrons able to attack to the microorganisms.

Scheme Scheme 1 depicts a representation of the main UV, visible, and nearIR charge excitation processes occurring in the ErW sample. The exact surface and bulk structures and defects and their influence in charge excitation and handling is not completely known. However, as demonstrated by the XAS/XPS combination, the local Er-W structures display differences at the surface and bulk. At bulk positions they have close Ti vacancies which would create electronic states able to accept charge under visible light excitation [2]. At the surface, W(Er)O$_x$ species with relatively low Er content (according to XPS) are relatively common due to the "high" W loading of the codoped material and the depletion of Er from the surface. Such species are excited by near IR photons and produce hot electrons able to attack the microorganisms [29,30].

4. Conclusions

The doping of a nanosized anatase (size near 10 nm) powder by tungsten and/or erbium was analysed in materials prepared by a microemulsion method. Both cations are presented at substitutional positions of the anatase structure rendering substitutionally disordered mixed oxides with anatase structure. More importantly, when both cations are present at the anatase structure, the local order is strongly modified by presence of a direct Er-O-W interaction and the corresponding charge neutrality defects. Surface and bulk structures/defects have a key but different role in producing charge carriers involved in the microorganisms attack.

The photocatalytic performance of these anatase-based materials was analyzed in the elimination of Gram-negative (*E. coli*) and Gram-positive (*S. aureus*) bacteria. Similar results are observed for both microorganisms, with an outstanding activity for the ErW sample. According to the kinetic analysis, this is grounded in the higher kinetic constant observed for this samples with respect to the rest of catalysts. Such a behavior is interpret on the basis of different physico-chemical phenomena for wavelengths above and below ca. 500 nm. Below this point the improvement of activity presented by the cooping sample seems closely connected with its unique structural (local order) properties which decreases charge recombination and increases the production of hydroxyl-type radical species. Above 500 nm the surface of the cooping material (and particularly W-containing suboxides) appears responsible of the creation of hot electrons able to inactivate the microorganisms. No important effect of IR to UV–vis up-conversion was noted in our samples.

Acknowledgements

References

[1] O. Carp, C.L. Huisman, A. Reller, Photoinduced Prog. Solid State Chem. 32 (2004) 33–117.
[2] A. Kubacka, G. Colón, M. Fernández-García, Chem. Rev. 112 (2012) 1555–1604.
[3] M. Peláez, N.T. Nolan, S.C. Pillai, M.K. Severy, P. Falaras, A.G. Kontos, P.S.M. Dunlop, J.A. Bryne, D.D. Dionysiou, Appl. Catal. B 125 (2012) 331–359.
[4] W. Choi, A. Termin, M.R. Hoffmann, J. Phys. Chem. 98 (1994) 13669–13703.
[5] A. Fuerte, M.D. Hernández-Alonso, A.J. Maira, M. Martínez-Arias, M. Fernández-García, J.C. Conesa, J. Soria, Chem. Commun. (2001) 2718–2721.
[6] M. Anpo, M. Takeuchi, J. Catal. 216 (2003) 505-318.
[7] A. Kubacka, M. Fernández-García, G. Colón, J. Catal. 254 (2008) 272–281.
[8] A. Kubacka, G. Colón, M. Fernández-García, Catal. Today 143 (2009) 286–292.
[9] M. Khan, Y. Song, N. Chen, W. Cao, Mater. Chem. Phys. 142 (2013) 148–153.
[10] D. Vanieri, F. Tournas, I. Gounaki, G. Kiriakidos, D. Matzavinos, J. Chem. Technol. Biotechnol. 92 (2017) 43–51.
[11] R. Asahi, T. Morikawa, T. Ohwaki, K. Aoki, Y. Taga, Science 293 (2001) 269–277.
[12] N. Serpone, J. Phys. Chem. B 110 (2006) 24287–24331.
[13] C. Belver, R. Bellod, S.J. Stewart, F.G. Requejo, M. Fernández-García, Appl. Catal. B 65 (2006) 309–314.
[14] M. Khan, S.R. Guly, J. Liz, W. Cao, Mod. Phys. Lett. B 29 (2015) 1550022.
[15] Q. Li, R. Xie, E.A. Mintz, J.K. Shang, J. Am. Ceram. Soc. 90 (2007) 3863–3868.
[16] B. Tryba, J. Hazard. Mater. 151 (2008) 623–627.
[17] A. Kubacka, B. Bachiller-Baeza, G. Colón, M. Fernández-García, Appl. Catal. B Environ. 95 (2010) 238–244.
[18] J.A. Rengifo-Herrera, C. Pulgarin, Solar Energy 84 (2010) 37–43.
[19] A. Kubacka, B. Bachiller-Baeza, G. Colón, M. Fernández-García, Appl. Catal. B Environ. 93 (2010) 274–281.
[20] V. Menendez-Flores, D.W. Bahnemann, T. Ohno, Appl. Catal. B Environ. 103 (2011) 99–108.
[21] Z. Zhang, S. Dai, M. Zhang, Y. Guo, J. Yang, J. Electrochem. Soc. 163 (2016) H42–H47.
[22] A.W. Xu, Y. Gao, H.Q. Liu, J. Catal. 207 (2002) 151–157.
[23] C.-H. Liang, M.-F. Hou, S.-G. Zhou, F.-B. Li, C.-S. Liu, T.-X. Liu, Y.-X. Gao, X.-G. Wang, J.-L. Lü, J. Hazard. Mater. 138 (2006) 471–478.
[24] S. Obregón, A. Kubacka, M. Fernández-García, G. Colón, J. Catal. 299 (2013) 298–306.
[25] J. Reszcynska, T. Grzub, J.W. Sobczak, W. Usowki, M. Gazda, B. Ohtani, A. Zalesca, Appl. Catal. B 163 (2015) 40–49.
[26] J. Reszcynska, T. Grzub, Z. Wei, M. Klein, E. Kowalska, B. Ohtani, A. Zalesca, Appl. Catal. B 181 (2016) 825–833.
[27] V.C. Bhethanabola, D.R. Ruseel, J.N. Kuhn, Appl. Catal. B 202 (2017) 156–164.
[28] D. Hin, R. Gown, X. Wang, P. Wang, T.-T. Lim, Appl. Catal. B 126 (2012) 121–133.
[29] Z. Lou, Q. Gu, L. Xu, Y. Liao, C. Xue, Chem. Asian J. 10 (2015) 1291–1299.
[30] J. Yan, T. Wang, G. Wu, et al., Adv. Mater. 27 (2015) 1580–1585.
[31] T. Matsunga, R. Tamada, H. Wake, FEBS Microbiol. Lett. 20 (1985) 211–216.
[32] J.C. Ireland, P. Klostermann, E.W. Rice, R.M. Clark, Appl. Environ. Microbiol. 53 (1993) 1668–1675.
[33] O.K. Dalrymple, E. Stefanakos, M.A. Trozt, D.Y. Goswany, Appl. Catal. B 98 (2010) 27–53.
[34] P.S.M. Dunlop, C.P.S. Sheeran, J.A. Bryne, M.A.S. McMahon, M.A. Boyle, K.G. McGuigan, J. Photochem. Photobiol. A 216 (2010) 303–338.
[35] M.A. Mahmood, S. Baruah, A.K. Anal, J. Dutta, Environ. Chem. Lett. 10 (2012) 145–162.
[36] C. Gou, K. Wang, S. Hou, L. Wang, J. Lv, Y. Zhang, X. Qu, S. Chen, J. Xu, J. Hazard. Mater. 323 (2017) 710–718.
[37] J. Kiwi, V. Nadtochenko, Langmuir 21 (2005) 4631–4641.
[38] R. Vinu, G. Madras, J. Indian Inst. Sci. 90 (2010) 189–203.
[39] H.A. Foster, I.B. Ditta, S. Varghese, A. Steele, Appl. Microbiol. Biotechnol. 90 (2011) 1847–1864.
[40] N.J. Sucher, M.C. Carles, T. Bak, Adv. Appl. Ceram. 111 (2012) 16–65.
[41] W. Wang, G. Li, D. Xia, T. An, H. Zhao, P.K. Wong, Environ. Sci. Nano 4 (2017) 782–799.
[42] J. Marugán, R. van Grieken, C. Sordo, C. Cruz, Appl. Catal. B 82 (2008) 27–34.
[43] A. Kubacka, M. Muñoz-Bastista, M. Ferrer, M. Fernández-García, Appl. Catal. B 140–141 (2013) 680–690.
[44] M. Fernández-García, X. Wang, C. Belver, J.C. Hanson, J.A. Rodríguez, J. Phys. Chem. C 111 (2007) 674–681.
[45] A. Le Bail, H. Duroy, J.L. Forquet, Mater. Res. Bull. 23 (1988) 447–455.
[46] G.K. Williamson, W.H. Hall, Acta Metall. 1 (1953) 22–31.
[47] K.V. Klementev, J. Phys. D: Appl. Phys. 34 (2001) 209–214.
[48] B. Cruz-Ortíz, J.W.J. Hamilton, C. Pablos, L. Díza-Jiménez, D.A. Cortés-Hernández, P.K. Sharma, M.A. Castro-Alférez, P. Fernández-Ibáñez, P.S.M. Dunlop, J.A. Byrne, Chem. Eng. J. 316 (2014) 179–186.
[49] J. Sambrook, E.F. Fritsch, T. Maniatis, Molecular Cloning: A Laboratory Manual, 2nd ed., Cold Spring Harbor Laboratory Press, 1989.
[50] M. Ferrer, J. Soliveri, F.J. Plou, N. López-Cortés, D. Reyes-Duarte, M. Christensen, J.L. Copa-Patiño, A. Ballesteros, Enzyme Microb. Technol. 36 (2005) 391–404.
[51] J.E. Dennis, D.M. Gay, R.E. Welsh, ACM Trans. Math. Software 7 (1981) 348–369.
[52] O. Lorret, D. Francova, G. Walderm, N. Stelzer, Appl. Catal. B 91 (2009) 39–46.
[53] D.-S. Kim, J.-H. Ysng, S. Balaji, H.-J. Cho, M.-K. Kim, D.-U.- Kang, Y. Djoued, Y.-U. Kwon, CrystEngComm 11 (2008) 1621–1629.
[54] N.W.J.Z. Bloh, A. Folli, D.E. Macphee, J. Phys. Chem. C 118 (2014) 21281–21292.
[55] M. Fernández-García, A. Martínez-Arias, A. Fuerte, J.C. Conesa, J. Phys. Chem. B 109 (2005) 6075–6083.
[56] Report on fitting procedures of the "error analysis committee" at http://ixs.csrri.iit.edu/IXS/subcommittee_reports/.
[57] J. Purans, A. Kuzmin, C. Guery, Proc. SPIE 2968 (1997) 174–179.
[58] L. Chen, T. Rajh, Z. Wang, M.C. Thurnauer, J. Phys. Chem. B 101 (1997) 10688–10696.
[59] D.L. Adler, D.C. Jacobson, D.J. Eaglesham, M.A. Marcus, J.L. Benton, J.M. Poate, P.H. Citrin, Appl. Phys. Lett. 61 (1992) 2181–21185.
[60] S.D. Shannnon, Acta Crystallogr. A32 (1976) 751–767.
[61] C.D. Wagner, W.M. Riggs, L.E. Davis, J.F. Moulder, G.E. Muilenber (Ed.), Handbook of X-Ray Photoemission Spectra, Perkin-Elmer, Minnesota, 1976.
[62] H. Irie, K. Kamiya, T. Shibanuma, S. Miura, D.A. Tryk, T. Yokohama, K. Hashimoto, J. Phys. Chem. C 113 (2009) 10761–10770.
[63] M. Fernández-García, A. Martínez-Arias, J.C. Hanson, J.A. Rodríguez, Chem. Rev. 104 (2004) 4063–4105.
[64] J. Castañeda-Contreras, V.F. Marañón-Ruiz, R. Chiu-Zárate, H. Pérez-Ladrón de Guevara, R. Rodríguez, C. Michel-Uribe, Mater. Res. Bull. 47 (2012) 290–299.
[65] G. Wang, W. Qin, J. Zhang, J. Zhang, Y. Wang, C. Cao, L. Wang, G. Wei, P. Zhu, R. Kim, Opt. Mater. 31 (2008) 296–302.
[66] C.-H. Liang, M.-F. Hou, S.-G. Zhou, F.-B. Li, C.-S. Liu, T.-X. Liu, Y.-X. Gao, X.-

G. Wang, J.-L. Lü, J. Hazard. Mater. 138 (2006) 471–478.

[67] D. Li, H. Haneda, S. Hishita, N. Ohashi, Chem. Mater. 17 (2005) 2596–2604.

[68] C. Mercado, Z. Seeley, A. Bandyopadhyay, S. Bose, J.L. McHale, ACS Appl. Mater. Interfaces 3 (2011) 2281–2288.

[69] I.R. Macdonald, S. Rhydderch, E. Holt, N. Grant, J.M.D. Storey, R.F. Howe, Catal. Today 182 (2012) 39–45.

[70] M. Fittipaldi, D. Gatteschi, P. Fornasiero, Catal. Today 206 (2013) 2–11.

[71] M.J. Muñoz-Batista, O. Fontelles-Carceller, M. Ferrer, M. Fernández-García, A. Kubacka, Appl. Catal. B 183 (2016) 86–95.

[72] Z. Lu, L. Zheng, W. Song, Z. Qin, D. Zeng, C. Xie, Appl. Catal. B 202 (2017) 489–499.

[73] D. Xia, W. Wang, Z. jian, T. An, G. Li, H. Zao, P.W. Wang, Appl. Catal. B 214 (2017) 23–33.

[74] S. Liu, D. Li, H. Sun, H.M. Ang, M.O. Tadé, S. Wang, J. Colloid Interface Sci. 468 (2016) 176–182.

[75] M.A. Grela, M.E.J. Coronel, A.J. Colussi, J. Phys. Chem. 100 (1996) 16940.

[76] A. Kubacka, M. Ferrer, M. Fernández-García, Appl. Catal. B 121–122 (2012) 230–238.

[77] E.G. Janzen, N. Sankuratry, Y. Kotake, J. Magn. Reson. 111 (1996) 254.

[78] M.D. Hernández-Alonso, A.B. Hungría, A. Martínez-Arias, M. Fernández-García, J.M. Coronado, J.C. Conesa, J. Soria, Appl. Catal. B 50 (2004) 167.

[79] D. Dvoranova´, V. Brezova´, M. Mazur, M.A. Malati, Appl. Catal. B 37 (2002) 91.

[80] C.F. Chignell, A.G. Motten, R.H. Sik, C.E. Parker, K. Reszka, Photochem. Photobiol. 59 (1994) 5–11.

[81] Q. Chen, H. Shi, W. Shi, Y. Xu, D. Wu, Catal. Sci. Technol. 2 (2012) 1213–1220.

[82] W. He, H. Jia, W.G. Wamer, Z. Zheng, P. Li, J.H. Callahan, J.-J. Jin, J. Catal. 320 (2014) 97–105.

[83] A. Kubacka, M. Ferrer, M. Fernández-García, C. Serrano, M.L. Cerrada, M. Fernández-García, Appl. Catal. B 104 (2011) 346–354.

[84] A. Kubacka, M. Suárez-Díaz, D. Rojo, R. Bargiela, S. Ciordia, I. Zapico, C. Barbás, A.P. Martins dos Santos, M. Fernández-García, M. Ferrer, Sci. Rep. 4 (2014) 4134–4142.

[85] T. An, H. Sun, G. Li, H. Zao, P.K. Wong, Appl. Catal. B 188 (2016) 360–366.

[86] T.A. Qui, B.M. Meyer, K.G. Christenson, R.D. Klaper, C.L. Haynes, Chemosphere 168 (2017) 1158–1168.

[87] G. Gogniat, M. Thyssen, M. Denis, C. Pulgarin, S. Dukan, FEMS Microbiol. Lett. 258 (2006) 18–24.

[88] S. Piegeot-R´emy, F. Simonet, E. Errazuriz-Cerda, J.C. Lazzaroni, D. Atlan, C. Guillard, Appl. Catal. B: Environ. 104 (2011) 390–398.

[89] M. Stucchi, C.L. Bianchi, C. Argirusis, P.M. Sakkas, V. Capucci, Appl. Catal. B 178 (2014) 124–132.